3-10-2004

Ion Based Pressure Sensor for Pulse Detonation Engines

Jeffrey S. Zdenek

ION BASED PRESSURE SENSOR FOR PULSE DETONATION ENGINES

THESIS

Jeffrey S. Zdenek, Captain, USAF

AFIT/GAE/ENY/04-M17

DEPARTMENT OF THE AIR FORCE
AIR UNIVERSITY

AIR FORCE INSTITUTE OF TECHNOLOGY

Wright-Patterson Air Force Base, Ohio

The views expressed in this thesis are those of the author and do not reflect the official policy or position of the United States Air Force, Department of Defense, or the U.S. Government.

AFIT/GAE/ENY/04-M17

ION BASED PRESSURE SENSOR FOR PULSE DETONATION ENGINES

THESIS

Presented to the Faculty

Department of Aeronautics and Astronautics

Graduate School of Engineering and Management

Air Force Institute of Technology

Air University

Air Education and Training Command

In Partial Fulfillment of the Requirements for the

Degree of Master of Science in Aeronautical Engineering

Jeffrey S. Zdenek, BS

Captain, USAF

March 2004

AFIT/GAE/ENY/04-M17

ION BASED PRESSURE SENSOR FOR PULSE DETONATION ENGINES

Jeffrey S. Zdenek, BS

Captain, USAF

Approved:

//signed//	10 Mar 2004
Ralph A. Anthenien (Chairman)	Date
//signed//	10 Mar 2004
Richard J. McMullan, Maj, USAF (Member)	Date
//signed//	10 Mar 2004
David E. Weeks (Member)	Date

Acknowledgments

I would like to express my sincere appreciation to my faculty advisor, Dr. Ralph Anthenien, for his guidance and support throughout the course of this thesis effort. His vast knowledge is not only the product of a sharp intellect, but a dedication that inspires us all.

I would like to thank Dr. Robert Hancock of AFRL/PRTS for funding and support to make this project possible.

The technical expertise of Mr. Andrew Pitts and Mr. Jay Anderson was also instrumental in the setup of this experiment.

Most importantly, I would like to thank my wife who never ceases to amaze me. She is the love of my life.

My family and friends have always been a source of strength for me and I thank them greatly.

Jeffrey S. Zdenek

Table of Contents

Page

Acknowledgments iv
Table of Contents v
List of Figures ix
List of Tables xii
List of Symbols xiii
Abstract xvi
I. Introduction and Overview 1
I.1 Chapter Overview 1
I.2 Motivation 1
I.3 Method 4
I.4 Thesis Content 6
II. Background and Theory 7
II.1 Chapter Overview 7
II.2 Ion Formation 7
II.3 Ion Decay 8
II.4 Internal Combustion Engines 9
II.4.1 Ignition Spark 10
II.4.2 Sensor Configuration 10
II.4.3 Combustion Conditions 11
II.4.4 Work of Saitzkoff et al. 13
II.4.5 Improved Model of Saitzkoff et al. 15

Page

II.5 Shock and Detonation Waves 17

II.6 Structure of the Pulse Detonation Wave 18

II.7 Comparison of Engine Times 20

II.8 Expected Ion Current in the PDE 21

II.9 Determining Pressure from the Ion Current in the PDE 22

II.10 Derivation of the Pressure and the Ion Current Decay Rate Relationship 22

III. Experimental Approach 26

III.1 Chapter Overview 26

III.2 Combustion Bomb 26

III.3 Ion Sensor 28

III.2.1 Short Probe 28

III.3.2 Medium Probe 29

III.4.3 Long Probe 30

III.4 Fuel and Air System 31

III.4.1 Methane 33

III.4.2 Dry Air 33

III.4.3 Vacuum Pump 33

III.4.4 Exhaust 34

III.4.5 Partial Pressure Control 34

III.4.6 Fuel & Air Procedure 35

III.5 Ignition System 35

Page

III.6 Instrumentation 37

III.6.1 DC Voltage for Ion Probes 38

III.6.2 Current Measurement 38

III.6.3 Pressure Sensors 40

III.6.4 Thermocouples 40

III.6.5 Band Heater 41

III.7 Data Flow 41

III.7.1 SCXI-1000 Chassis 42

III.7.2 NI 6024E DAC 43

III.7.3 NI 6110 DAC 44

III.7.4 Labview Program 44

III.7.4.1 Program Modes 44

III.7.4.2 DAC Drivers 45

III.7.4.3 Triggers 45

III.7.5 Acquisition Rates 46

III.8 Shielding 46

III.9 Steady State Ion Current Experiment 47

III.10 Transient Ion Current Experiment 48

III.11 Combustion Experiment 49

III.11.1 Initial Conditions 49

III.11.2 Test Cases 49

Page

III.11.3 Test Procedure 52

IV. Raw Data 53

IV.1 Chapter Overview 53

IV.2 Measurement Error 53

IV.3 Results of Raw Data 54

V. Data Reduction and Discussion 64

V.1 Chapter Overview 64

V.2 Analysis of Raw Data 64

V.3 Error Analysis 66

V.4 Reduced Data as a Function of Time 67

V.5 Influence of Equivalence Ratio 74

V.6 Results as a Function of Pressure 77

V.7 Probe Resolution 84

VI. Conclusions 85

VI.1 Conclusions 85

VI.2 Future Work 86

VI.3 Future Experimental Setup Recommendations 86

Appendix A: LabView Program 88

Bibliography 93

Vita 95

List of Figures

Page

Figure 1. ZND Detonation wave structure moving from left to right..... 19

Figure 2. Overview of Experiment Configuration..... 27

Figure 3. Champion RC12LYC Spark Plug 28

Figure 4. Short Probe with side prong of RC12LYC spark plug removed..... 29

Figure 5. Medium Probe with 2.54 cm center electrode..... 30

Figure 6. Long Probe with 10.16 cm insulated extension..... 31

Figure 7. Fuel and air system block diagram..... 32

Figure 8. Ignition Circuit 36

Figure 9. Ion Probe Circuit 39

Figure 11. Runs at the baseline case of φ = 1.0 at an initial pressure of 3 atm..... 55

Figure 12. Comparison of 5V, 10V, & 40V across the ion probe at 56

an initial pressure of 3 atm and φ = 1.0 56

Figure 13. Effects of φ = 0.7, 1.0, & 1.2 at initial pressure of 1 atm..... 57

Figure 14. Effects of φ = 0.7, 1.0, & 1.2 at initial pressure of 3 atm..... 58

Figure 15. Effects of φ = 0.7, 1.0, & 1.2 at initial pressure of 5 atm..... 59

Figure 16. Effect of initial pressures of 1, 3, & 5 atm at φ = 1.0..... 60

Figure 17. Zoomed in view of Figure 16, effects of initial pressure of 1, 3, & 5 atm at φ = 1.0..... 61

Figure 18. Effects of probe length at baseline case of φ = 1.0 at 3 atm..... 62

Page

Figure 19. Zoomed in view of Figure 18 more clearly showing the effects of probe length at the baseline case of φ = 1.0 at 3 atm 63

Figure 20. Averaged Current and Pressure for initial pressures of 1, 3, & 5 atm at φ =1.0 67

Figure 21. Saitzkoff et al. model applied to this experiment at baseline condition of 3 atm initial pressure and φ = 1.0 69

Figure 22. Current and derivative at baseline case 70

Figure 23. Filtered derivative and current at baseline case 71

Figure 24. Repeatability of filtered derivative for 3 runs at baseline condition 72

Figure 25. Filtered derivative compared for several initial pressures at φ = 1.0 73

Figure 26. Expanded view of Figure 25 showing pressure affects on the derivative 74

Figure 27. Effect of equivalence ratio on maximum ion current for initial pressures of 1, 3, & 5 atm 75

Figure 28. Peak decay rate of current as a function of equivalence ratio for initial pressures of 1, 3, & 5 atm 76

Figure 29. Maximum current averaged over three test runs plotted against the instantaneous pressure at φ = 1.0 78

Figure 30. Maximum current for individual runs compared to pressure. The trend line shows the correlation computed from averaged cases 79

Figure 31. Peak decay rate averaged over three test runs and compared against instantaneous pressure for cases of φ = 1.0 80

Page

Figure 32. Peak decay rate for individual cases compared to the instantaneous pressure. A new correlation is computed. 82

Figure 33. First program mode front panel 89

Figure 34. First mode front panel showing ion current in frequency domain 90

Figure 35. Top section of block diagram for first mode 90

Figure 36. Bottom section of block diagram for first mode 91

Figure 37. Front panel for second mode 91

Figure 38. Top section of block diagram for second program mode 92

Figure 39. Bottom section of block diagram for second mode 92

List of Tables

Page

Table 1. Test cases for medium probe at +10 V DC 50

Table 2. Test cases for long probe at +10 V DC 50

Table 3. Test cases for short probe at +10 V DC 51

Table 4. Test cases at various voltages at 3 atm and φ = 1.0 51

Table 5. Percent Error in Equivalence Ratio 66

List of Symbols

Abbreviations

AC = Alternating Current

atm = Atmospheres

cm = Centimeters

DAC = Data Acquisition Card

DC = Direct Current

eV = Electron Volt

FFT = Fast Fourier Transform

Hz = Hertz

IC = Internal Combustion

in = Inch

K = Kelvin

kHz = kilo-Hertz

kΩ = kilo-Ohm

kS/s = kilo-Samples per Second

m = Meter

MB = Mega-Byte

MHz = mega-Hertz

ms = milli-Second

MS/s = mega-Samples per Second

mV = milli-Volt

PID = Proportional-Integral-Derivative

psi = Pounds per Square Inch

psia = Pounds per Square Inch Absolute

psig = Pounds per Square Inch Gauge

PDE = Pulse Detonation Engine

PDRE = Pulse Detonation Rocket Engine

rpm = Revolutions per Minute

RMSE = Root Mean Square Error

RSS = Root of the Sum of the Squares

s = Second

ZND = Zeldovich, von Neumann, and Doring

μA = micro-Amp

μs = micro-Second

˚C = Degrees Celsius

φ = Equivalence Ratio

Ω = Ohm

Symbols

A = Exposed Surface Area of Probe

E = Electric Field

I = Current

n = Number Density of Charge Carriers

P = Pressure

q = Elementary Charge ($1.60 \text{ X } 10^{-19}$ Coulumb)

R = Resistance

t = time

T = Temperature

τ = Mean Free Time

v_{avg} = Average Electron Velocity

v_d = Electron Drift Velocity

V = Volts

Abstract

A high speed durable ion probe based pressure sensor is being investigated for use in pulse detonation engines. The environment encountered in such engines necessitates high temperature and durable (vibration resistant) devices. Traditional pressure sensors can be used however, various methods and materials used to protect the sensors dampen and reduce the pressure wave allowing for qualitative results only. An alternative transient pressure sensing method is investigated for pressures behind a hydrocarbon flame in the pulse detonation engine. Hydrocarbon flames generate ions that are quenched by collisions with other species and walls. As the collision rate is a function of pressure, so too is the ion decay rate. The ion decay rate is measured using an ion probe that is well suited for high temperature flow, has no moving parts, and is inexpensive. Similar systems have been used to determine multiple combustion conditions in automobile engines. This investigation builds upon these capabilities to examine the quantitative pressures. The ion probe measures the ionization in the form of a small current. The strength of the ion current indicates the strength of the ionized field which decays according to pressure. An experiment was devised to correlate the ion current decay rate with the pressure. A correlation has been established showing pressure is a function of the ion current decay rate. This investigation shows a viable alternative method for measuring pressure in the pulse detonation engines although additional work is required to improve the accuracy of the method.

ION BASED PRESSURE SENSOR FOR PULSE DETONATION ENGINES

I. Introduction and Overview

I.1 Chapter Overview

This chapter describes the need for an improved pressure sensor for the pulse detonation engine. The methodology for making this improvement is also explained.

I.2 Motivation

The United States Air Force, along with other organizations, is currently investigating the Pulse Detonation Engine (PDE) as a future propulsion system. While not a new concept, the engine is still in developmental stages. The PDE theoretically offers higher efficiency with less complexity and lower weight than the turbofan engines in use today. In addition to air-breathing cycle, the PDE can also operate as a rocket cycle termed the Pulse Detonation Rocket Engine (PDRE). The PDE and PDRE are also attractive due to their large flight envelope: from static up to around Mach Number 5. Turbofan designs are typically limited to Mach Number 2 or 3. On the other hand, ramjets and scramjets require supersonic speeds in order to start producing thrust. The large flight envelope of the PDE eliminates the need for any boosters.

The basis for the PDE is the higher efficiency of a detonation combustion process compared to the constant pressure deflagration process used in conventional turbomachinery based air-breathing engines of today. This efficiency comes from the

near constant volume process and the fact that the PDE does not require the working fluid to be compressed prior to heat addition. Although unsteady, this process closely follows the thermodynamics of a Humphrey constant-volume cycle [6]. Simple theoretical calculations show the efficiency of the Brayton, Humphrey, and Chapman-Jouguet Detonation cycles to be 27%, 47%, and 49% respectively [6]. Compared to the constant pressure Brayton cycle, the Humphrey cycle achieves higher efficiency by creating higher temperatures at lower entropy. In addition to the clear thermodynamic advantages, the PDE also has the potential to reduce cost and enhance performance without the heavy turbomachinery in conventional air-breathing engines.

Conventional turbomachinery based engines use a steady process of compression, heat addition, and expansion to generate thrust. The pulse detonation engine generates thrust through an entirely different unsteady process. PDE is similar in many ways to internal combustion (IC) engines. Like the IC engine, the PDE fills a tube with air and then adds fuel creating a near stoichiometric mixture. In the IC engine, the piston compresses the mixture and initiates deflagration using a spark plug. In the PDE, no compression is required. The fluid can also be ignited with a spark plug, but deflagration instead transitions to detonation as the combustion moves down the tube. This detonation wave is the basis of the PDE. Detonation by nature is an unsteady process where the wave, according to Chapman-Jouguet theory, travels at supersonic speeds relative to the unburned fuel-air mixture. The PDE takes advantage of this unsteady process by employing multiple detonation tubes similar to multiple cylinders in an IC engine. Each

tube, similar to the 4 stroke cycle in IC engines, is either being filled with the fuel-air mixture, detonating the mixture, blowing down, or purging the exhaust.

In order for a successful detonation near Chapman-Jouguet predicted speeds, the combustion must produce a strong shock wave that travels down the tube. This shock wave increases the temperature and pressure of the fuel-air mixture. After a short induction period, this mixture combusts or detonates in a thin region behind the shock wave. The detonation then creates the even higher temperatures and pressures needed to sustain the shock wave.

Each detonation wave produces a small amount of thrust based on the diameter of the tubes, the speed of the detonation wave, and the pressure behind the wave. Since the PDE is unsteady, the rate of firing each tube directly affects the generation of thrust. Substantial gains in thrust can be achieved by increasing the cycle frequency. At higher frequencies, however, timing becomes critical to successful detonations. Although the deflagration to detonation transition has been heavily researched, in practice wave speeds near Chapman-Jouguet theory are not always realized. Often, weaker shock waves are formed resulting in substantially slower wave speeds. These weak detonations greatly reduce thrust of the engine.

Despite recent progress, significant challenges remain before reliable PDE operation with practical fuels is realized [11]. Further, the cycle creates higher temperatures than the Brayton cycle leading to high heat loading [10]. As PDEs increase their cycle frequency, heat loads increase [10] thus heat related problems will only worsen. These high temperatures limit the diagnostic tools available to researchers.

Specifically, conventional piezoelectric based pressure transducers are ill-suited for the high temperatures and harsh vibratory environment within the PDE. A variety of techniques can be used to increase the useful limits of the piezoelectric pressure transducers. Each of these techniques have disadvantages that often skew the results. For example, protective ablative coatings on the pressure transducers improve the resistance to the harsh environment but reduce the sensitivity. These coatings reduce the effectiveness of the pressure transducer as a quantitative instrument because of the inherent dampening of the materials. Accurate compensation for the dampening effects is not feasible due to the variability in the thickness of the material as well as the ablation rate itself. For single firings of a detonation tube this ablation can be measured and added as a correction factor to the pressure measurement. In steady operation, measuring the ablation of the protective material is not feasible. A durable, quick response quantitative pressure sensor is needed to optimize the PDE during development, and also to provide feedback for engine control.

I.3 Method

IC engines have also encountered similar problems with measuring pressure within the cylinder. Sensing the cylinder pressure enables tighter control of equivalence ratio (φ) leading to reduced hydrocarbon emissions [15]. Equivalence ratio by definition is the air to fuel ratio divided by the air to fuel ratio at stoichiometric conditions. While various techniques exist for developmental engines, modifying production engines to include a reliable pressure sensor is not practical. Production engines have no place to install extra high-cost sensors. Using these conventional sensors can change the

combustion in the cylinder and require, similar to the PDE, a complex cooling system [21]. The sensors and modifications are not practical for long-term use needed for production engines. In order to solve this problem, several techniques have been developed to extract information from the ionization resulting from the combustion process. By placing a small direct current (DC) voltage across the gap after discharge, the spark plug acts as an ion sensor. This ionization then produces a small ion current across the spark plug gap after the ignition. Without any modifications within the cylinder, information can be extracted from the ion current. To date, the spark plug has controlled the equivalence ratio [15], detected misfire [3], and controlled knock [3]. Additionally, the spark plug has been employed to measure pressure in the cylinder [19]. In short, internal combustion engines have utilized the ion current across the spark plug to measure several important conditions.

Applied to the PDE, the spark plug already acts as a rugged ion sensor to measure wave speed [22, 23]. Two spark plugs with an applied DC voltage are inserted a known distance apart in the PDE tube. The measurement is made by determining the time delay between the voltage discharges of two spark, resulting in a simple, but highly useful method for determining average detonation wave speed [22, 23].

The spark plug has already proven its durability to the harsh PDE environment. Extending the use of the spark plug to measure pressure in the PDE is a logical improvement. By utilizing the advancements in IC engines, the spark plug can be employed to a much greater extent in the PDE and become an additional pressure

transducer. Before this extension can be put to use, the underlying theory must be tested for conditions in the PDE and several engineering challenges overcome.

I.4 Thesis Content

This thesis covers the experimental work completed in adapting the spark plug as a pressure sensor in the PDE. Previous work and the theoretical basis of this investigation are described in Chapter II. The progress made in using the spark plug as an ion sensor in internal combustion engines is leveraged and applied to this investigation. Based on the previous work, predictions are made on how the decay rate of the ion current is a function of pressure. In order to test this prediction, an experimental approach is devised. The details of the approach including the instrumentation and data capture are described in Chapter III. The raw results from this testing are shown in Chapter IV along with a short discussion on the observed phenomena. The data is then analyzed and reduced in Chapter V. An error analysis is accomplished to determine the accuracy of the data. The predictions of Chapter II are compared to the analyzed data in Chapter V and the overall accuracy of this method is addressed. Conclusions of this investigation are described in Chapter VI.

II. Background and Theory

II.1 Chapter Overview

This chapter describes the work of others in understanding the theory on how to determine pressure from the ion sensor. This knowledge is then applied to the problem at hand by predicting how the sensor will function.

II.2 Ion Formation

It is well known that hydrocarbon flames have conductive properties. Considerable research over several decades has investigated the formation of ions in flames [8]. The formation of these ions within the flame is attributed to the chemi-ionization reactions [4]. These reaction are not initial reactants and products but intermediate short lived species of the combustion process. One important example being [5]:

$$CH + O \rightarrow CHO^{+} + e^{-} \quad (1)$$

Other typical reactions include [3,21]:

$$CHO^{+} + H_2O \rightarrow CO + H_3O^{+} + e^{-} \quad (2)$$

$$CH + C_2H_2 \rightarrow C_3H_3^{+} + e^{-} \quad (3)$$

Many other reactions are important in chemi-ionization and models for ionization can be very complex. Because these reactions and species can vary greatly depending on the initial and local conditions, the chemi-ionization process can be extremely complex. Extensive research has investigated these species and reactions. In a laboratory setting important reactions and species can be identified. Unknowns and local variability in the PDE, however, preclude the detailed examination of individual species and reactions. Instead, the ions will be considered at a global level for the development of a useful pressure sensor in the PDE.

Under local thermal equilibrium conditions, the ion concentration, as a function of temperature, is given by Saha's equation:

$$\frac{n_i n_e}{n_{i-1}} = 2\left(\frac{2\pi m_e kT}{h^2}\right)^{\frac{1}{2}} \frac{B_i}{B_{i-1}} \exp\left[-\frac{E_{ion}}{kT}\right] \tag{4}$$

The reactions, as shown by the example in Eq. (1), in a hydrocarbon flame, place the ion concentration at super-equilibrium levels.

II.3 Ion Decay

The net rate change of ion concentration is the difference between the production and recombination rates of reaction. Typical recombination reactions are given by [3, 5]:

$$\begin{aligned} H_3O^+ + e^- &\rightarrow H_2O + H \\ &\rightarrow OH + 2H \end{aligned} \tag{5}$$

The super-equilibrium ion concentration will naturally decay to the levels governed by Eq. 4 through molecular collisions. As the recombination reaction has a molecularity of two, the rate of ion decay is therefore dependent on the square of pressure [4].

By measuring the ion density as a function of time it is possible to determine the pressure. While the pressure could be theoretically determined in any region of ion concentrations above equilibrium, practicality limits the regions for useful measurement. While ion production can be predicted in a tightly controlled laboratory setting where highly sensitive initial and local conditions can be determined, implementing these measurements into the PDE is not practical. The pressure measurement can be simplified if the decay is observed well past the ion generating reaction front so that only the recombination reaction rate need be considered.

II.4 Internal Combustion Engines

The various methods in IC engines have already used these chemi-ionization relationships to successfully measure various properties of combustion [3, 17, 21]. Some methods refer to a flame resistance instead of an ion current. The flame resistance is inversely proportional to the ion current based on Ohm's Law:

$$R = \frac{V}{I} \tag{6}$$

where V is the voltage, I is the current, and R is the flame resistance.

Since the IC engine methods use the spark plug both for combustion ignition and ionization detection, careful consideration must be given to prevent the ignition system from interfering with the ion sensing. The PDE setup can avoid some of the complications of the IC systems by separating the ignition and ion sensing functions. Many significant results can be directly incorporated for use in the PDE.

II.4.1 Ignition Spark

In some cases, the ion current may be obscured by the spark. The spark is the result of the breakdown of the local air and fuel mixture into plasma by a strong electric field. During the spark, the electric field and plasma will dominate the current measurement resulting in large current variations not based on ion production. The sensor values during the spark must therefore be discarded when solely trying to measure the current due to ionization. A short time period after the spark, the measured current can be considered dominated by the ionization of the mixture.

II.4.2 Sensor Configuration

Some results from IC engines can be directly applied to the PDE. **A**pplying a positive DC voltage captured a larger quantity of ions than a negative DC bias because of the higher mobility of the electrons compared to the positive ions [21]. Further, the detection sensitivity improved when increasing the surface area of the center electrode on the spark plug [17].

II.4.3 Combustion Conditions

When testing several Air/Fuel ratios, results, for an engine running at 2570 revolutions per minute (rpm), showed the flame resistance was at a minimum when the peak internal pressure was at a maximum [17]. A low flame resistance corresponds to a high current through Ohm's Law and shows that actual ionization levels are highest near stoichimetric conditions. At this engine speed the combustion and post-combustion zones occur on the order of 12 milliseconds (ms) assuming a change in crank angle of 90 degrees. Results also showed that the intake pressure does not change the flame resistance significantly [17]. This finding reinforces the fact that the ionization is due to the chemi-ionization and not initial pressure.

Additional work examined the use of ionization current to adjust timing in an IC engine [7]. One ionization measurement system is already in use in a SAAB engine [7]. IC engines use a peak pressure algorithm for ignition timing [7]. These algorithms are constrained by the thermal and high pressure limits of pressure sensors [7] and could be improved by using the ion current across the spark plug as a feedback sensor to determine peak pressures. Ionization current can be affected by temperature, air-fuel ratio, time since combustion, exhaust gas recycling, fuel composition, engine load, etc [7]. Despite complications, results show typical ionization curves for ignition, flame front, and post flame. In the post flame region, relatively stable ions follow the cylinder pressure trend [7]. NO was found to be a contributor to the post-combustion ionization because of the low ionization energy [7]. A Gaussian function for the ion current was developed based on the pressure [7]. Problems arise when trying to extract pressure information from

ionization current [7]. A peak pressure search is not feasible since the flame-front often has more than one peak and the post-flame zone doesn't have a peak [7]. To address the problem of flame fronts with two peaks, two Gaussian models were used for the flame front and one for the post flame phase [7]. This technique captured the structure of the ionization current although quantitative comparison was not provided [7].

Relatively few experiments have been conducted in a combustion bomb whereas most experiments have been conducted using gasoline IC engines. A constant volume combustion bomb experiment was conducted to investigate the use of the spark plug as a combustion probe mainly to estimate combustion quality [2]. The approach only addressed the question of combustion quality and not the underlying combustion phenomena [2]. Several signal processing methods were used in this analysis. Pattern recognition and classifier design were used to perform signal classification [2]. Classification also was accomplished by artificial neural networks using Matlab [2]. In addition to the combustion bomb experiment, tests were also conducted with internal combustion engines. This experiment concludes that a nonlinear relationship exists between ionization current and combustion quality [2]. Results showed that the spark plug can be a reasonable ionization probe as long as efficient signal processing algorithms are used [2].

Further work shows that the ionization closely follows the pressure variation in time scales of milliseconds in a combustion bomb setup [1]. Temperature is assumed to be a known function of time. In a combustion bomb, the rate of rise of temperature

determines the maximum value of the ionization current [1]. The current is also very sensitive to the air-fuel ratio. At high air-fuel ratios, the current quickly decreases.

II.4.4 Work of Saitzkoff et al.

Saitzkoff et. al. [18] investigated the use of the spark plug as an ionization sensor for internal combustion engines. Their work assumes thermodynamic equilibrium conditions after complete combustion where the gas is undergoing adiabatic expansion. The test V6 engine ran at 1300 rpm at full load. At this engine speed the combustion and post-combustion zones occur on the order of 23 ms assuming a change in crank angle of 90 degrees. By applying a 80 volt DC to the spark plug the measured voltage was converted into current across a known 22 kiloOhm (kΩ) resistance with an estimated error of 5% [18]. An adiabatic maximum flame temperature of 2800 Kelvin (K) was assumed at a maximum pressure of 5.7 MPa (56.25 atm) [18]. Saitzkoff et al. assume Nitric Oxide (NO) to be the dominate ionization molecule due to a low ionization energy of 9.27 electron Volts (eV) [18]. NO is formed by means of the extended Zeldovich mechanism [14].

$$O + N_2 \leftrightarrow NO + N \quad (7)$$

$$N + O_2 \leftrightarrow NO + O \quad (8)$$

$$N + OH \leftrightarrow NO + H \quad (9)$$

NO can also be formed by the low temperature “prompt” or Fenimore NO_x mechanism. High NO formation rates exist near the combustion zone due to super-equilibrium levels

of O and OH radicals [18]. Since the combustion zone is thin at these high pressures, Saitzkoff et al. assume the formation of NO near combustion to be small compared to formation in the post-combustion zone and therefore unimportant in their model [18]. The NO concentration in the post-combustion zone is assumed to be 1% [18]. Based on this assumption, Saitzkoff et al. claim that the source of the free electrons is not chemical reactions but thermal ionization [18].

Using the thermal ionization assumption, Saitzkoff et al. derived an ionization model using Saha's equation (4), the ionization ratio of the particles, and the electron drift velocity [18]. Within this model, the normalized current and pressure values were related by the following [18]:

$$\frac{I}{I_{\max}} = \frac{1}{\left(\frac{P}{P_{\max}}\right)^{\frac{1}{2}-\frac{3\gamma-1}{4\gamma}}} \exp\left[-\frac{E_i}{2kT_{\max}}\left(\left(\frac{1}{\left(\frac{P}{P_{\max}}\right)^{\frac{\gamma-1}{\gamma}}}\right)-1\right)\right] \tag{10}$$

Calculated pressures were correlated to the post-flame ionization peak due to NO production [18]. A low signal-to-noise ratio required the current to be filtered before making calculations and data was averaged over 50 cycles [18]. Although equation (6) is sensitive to the temperature because of the exponential term, Saitzkoff et al. found the experimental relative values to be slightly higher than predicted but still in fair agreement [18].

Saitzkoff et al. state their ionization model is only applicable to the post-combustion zone [18] but contradict themselves by applying the model to the full crank angle limits. This limitation causes poor prediction of the ion current during combustion as expected but still agrees with the post-flame ionization peak. At these high load test cases, high temperature creates the needed activation energy for the NO. The low engine rpm allows NO the relatively long chemically kinetic formation time. The high pressure produces a high partial pressure of NO thus increasing the ion density. At these specific conditions the assumption that post-flame ionization is dominate is valid. Despite neglecting chemi-ionization, an additional smaller, although still prominent, ionization peak occurs before the post-combustion peak [18]. At lower engine loads the lower temperatures will decrease the level of thermal ionization and could allow the chemi-ionization peak within the combustion zone to become dominate. Depending on combustion conditions either or both ionization peaks may be important.

II.4.5 Improved Model of Saitzkoff et al.

In follow-on work, Saitzkoff et al. [19] sought to improve the results of trying to predict pressure with the ion current across the spark plug. Saitzkoff et al. [19] again focused on the post-flame zone where the gas species are assumed to be in chemical equilibrium and only thermodynamic conditions are changing. They identified, however, an additional smaller ionization peak above thermal ionization levels due to the chemi-ionization processes at the flame front [19]. They relax previous assumptions to allow species with low ionization energies, such as long lived hydrocarbons, to chemically react and influence the ion current in addition to thermal equilibrium levels [19]. A zero-

dimensional chemical kinetic model was used with 64 species and 268 reactions [19]. The extended Zeldovich mechanism was used for NO calculations. In order to accommodate the entire engine load spectrum, the drift velocity was determined using both the thermodynamic conditions and the electric field [19]. For these tests, the electric field was 80 kV/m. Slightly different expressions result for the ion current depending on which force dominates [19]. In the region where both forces are important, a weighted linear combination is applied [19]. Both positive and negative ions are examined in the chemical kinetic model. Negative ions are also governed by Saha's equation (5) through the example reaction:

$$M^- + E'_{ion} \rightarrow M + e^- \tag{11}$$

where the negative ion (M^-) is in a ground state and E'_{ion} is the energy require to neutralize the negative ion [19]. The current will be the summation of electrons, positive ions, and negative ions [19]. This method is complicated by the fact that the ionization depends upon the thermodynamic state that the sensor is trying to detect [19]. Therefore additional information and assumptions are required to solve the problem [19]. Finally, a range of engine velocities, throttle positions, torques, ignition timings, and lambda are investigated to experimentally validate the improved model [19].

Using the previous model, the peak values for ion current and pressure are correlated and the correlation coefficient is found to be 0.6 [19]. The "not particularly high" [19] coefficient is the result of erratic ion currents for each cycle. Saitzkoff et al.

[19] found that the ion current decreased at lower equivalence ratios when results were averaged over 500 cycles. At leaner mixtures the NO concentration increases and therefore the ion current is expected to increase as well. The reason for the decreasing ion current at leaner mixtures is the decrease in temperature and therefore lower ionization ratios [19]. The dominant electronegative species was found to be the hydroxyl radical (OH) [19]. Results show long lived hydrocarbon species are not important to the ion current [19]. Electrons were found to be the dominant charge carrier due to the higher drift velocity resulting from their lower mass [19]. Saitzkoff et al. also found a strong correlation in time between the maximum peak current in the post-combustion region and the maximum peak pressure [19]. Slight differences were explained by the difference between the maximum pressure of the gas and the maximum density [19]. Over a large number of cases the correlation coefficient of 0.8 was obtained without filtering of the current [19]. Although low load driving conditions had low correlations, in averaged cases the correlation of predicted pressure was above 0.95 [19]. Overall Saitzkoff et al. showed that pressure can be predicted by the ion current although not currently as accurate as desired.

II.5 Shock and Detonation Waves

The flame structure in both space and time can be highly turbulent especially when interacting with waves [14]. This complexity was examined for detonation waves in hydrogen-oxygen mixtures [14]. Results for detonation waves show the shock has little influence on the ionization compared to the flame or the detonation wave [14]. In a hydrogen-oxygen mixture with 1.0 percent N_2 the conductivity was found to be 4.5×10^{-4}

and 4 x 10^{-5} (ohm cm)$^{-1}$ for the detonation and flames respectively [14]. Conversely, the shock conductivity was several orders of magnitude lower at 5.4 x 10^{-13} (ohm cm)$^{-1}$ [14]. Combustion will therefore produce ionization levels nine orders of magnitude larger than a shock alone. The shock ionization was attributed to purely thermal equilibrium values [14]. NO also dominates the ion-producing species behind detonations [14]. Some impurities, however, could become highly ionized and obscure the ionization distinctions between flames, detonations and shocks [14]. Assuming effects of impurities are insignificant, the generation of ions by the shock can be considered negligible. The ionization behind the detonation wave should also be larger than ordinary flames.

II.6 Structure of the Pulse Detonation Wave

While the physical time and space structure of a detonation wave is extremely complex three dimensional phenomena, the one dimensional theoretical structure as described by Zeldovich, von Neumann, and Doring, referred to as ZND wave structure [6], is relatively straightforward as shown in Figure 1.

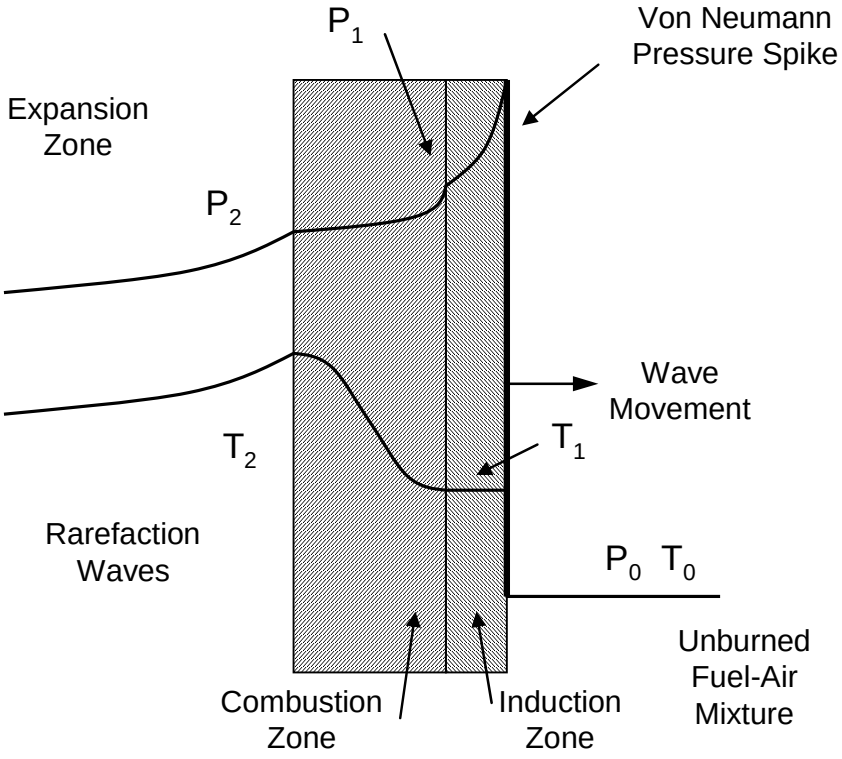

Figure 1. ZND Detonation wave structure moving from left to right

The detonation wave begins near the closed end of the tube and travels through the unburned fuel-air mixture towards the open end of the tube. The fuel-air mixture first encounters a strong shock wave that compresses the mixture, elevating both the temperature and pressure [6]. After a short ignition delay, or induction zone, the combustion initiates creating Rayleigh type heat addition into the flow [13]. Once the combustion is complete at state 2, the flow is at Chapman-Jouguet conditions for a self-sustaining detonation [6]. The shock wave and combustion zone are closely coupled phenomena necessary for a detonation wave. The speed of the wave relative to the burned mixture is sonic, whereas relative to the unburned mixture the wave is supersonic. The

speed of the wave is driven by the heat release rate of the combustion. A large pressure spike, termed the von Neuman spike, occurs immediately behind the shock wave [6]. As the wave passes, the flow expands to the level of the closed end through rarefaction waves [6].

The total width of the shock, induction zone, and combustion zone is on the order of one centimeter [6]. Measured wave speeds of 1957 meters per second (m/s) were produced from the Air Force Research Lab, Propulsion Directorate PDE (AFRL/PRTS) [20]. Therefore, the time for the detonation wave to travel a 1 meter tube is on the order of 0.5 ms. The time for the entire detonation wave structure, assuming a length of 1 cm, to pass a point in the tube is on the order of 15 microseconds (μs) or 66 kilohertz (kHz) [6]. The shock wave itself has a length of several molecular mean free paths ($6 \text{ X } 10^{-8}$ m) resulting in a time on the order of 30 picoseconds (fs) or 33 gigahertz (GHz) to pass a point in the tube. Assuming the time for expansion is larger than the detonation wave travel time, the time for the pressure to decay from state 2 to the closed end wall is on the order of 1 ms.

II.7 Comparison of Engine Times

IC engines and the PDE operate on different time scales. Depending on the speed of the IC engines, the combustion and post-combustions time is on the order of 20 ms whereas the PDE is on the order of 1 ms. The PDE is roughly one order of magnitude faster than IC engines. Laminar flame speed in air, for comparison, is on the order of 0.7 m/s for hydrocarbons and 0.4 m/s for methane [12:130-131]. Detonation waves are

therefore three and a half orders of magnitude faster than laminar flame speeds. These different time scales play an important role in ionization and measurement techniques.

II.8 Expected Ion Current in the PDE

The initial ionization level is extremely small in low temperature regions such as the unburned mixture in the PDE before the arrival of the detonation wave. The shock wave increases the degree of ionization through thermal heating and remains roughly constant through the induction zone. As previously discussed, the combustion zone sharply increases the ionization level by nine orders of magnitude higher than the shock wave, due to both chemi-ionization and thermal effects at elevated temperatures. This high super-equilibrium ionization level will then decay down to equilibrium levels at lower temperature.

The low ionization levels in the unburned fuel-air mixture will make the measurement of an ion current above the noise extremely difficult. The first increase in ion current would be created from the shock. The short lengths of the shock and induction periods make measuring this current impractical. The combustion zone will create a large increase in the ion current. The ion current decay rate from this super-equilibrium level is a function of the square of pressure through molecular recombination. The pressure during the expansion region could be determined by measuring the ion decay rate and correlating it to the pressure.

II.9 Determining Pressure from the Ion Current in the PDE

This method could provide useful pressure information between state 2, as shown in Figure 1, and the closed end wall. The von Neumann pressure spike would be impractical to measure due to the short duration and low ionization level compared to the end of the combustion zone. Because this method relies upon the ion decay and not equilibrium concentrations, the method can only be applied to unsteady processes and not steady state conditions typically measured by conventional piezoelectric pressure transducers. Like the IC engines, the ion current in the PDE can also be measured using a spark plug. The durability of the spark plug is inherently suited for the harsh environment of the PDE.

The ion current in the PDE, unlike the IC engines, should not experience a second ionization peak due to NO formation. Although NO is still the dominate ion producing species behind detonation waves, the relative concentration is lower than in IC engines. The order of magnitude quicker processes of the detonation wave and expansion zone provide less time for the slow chemical kinetics to form NO. Further, the lower pressures in the PDE will lower the partial pressure and thus density of any NO produced. Chemi-ionization will be the dominant factor in ion production for the PDE.

II.10 Derivation of the Pressure and the Ion Current Decay Rate Relationship

A simple derivation can show how the decay rate of the ion current relates to the pressure. The electric current I, by definition, is the rate that charge passes through a surface. In this case the surface is the exposed area of the ion probe. Current can also be expressed in the form:

$$I = nAv_d|q| \tag{12}$$

where n is the number density of the charge carriers, A is the surface area of the probe, v_d is the drift velocity and q is the charge. Assuming the net motion is due to the electric field, an ion can be accelerated by the electric field until it collides with another molecule. The average speed of the electrons is not considered because the velocity after collision is randomly directed and does not contribute to the drift velocity. The drift velocity is then expressed by:

$$v_d = \frac{|q|E\tau}{m} \tag{13}$$

where E is the electric field, m is the mass of the electron, and τ is the mean free time. The mean free time is simply:

$$\tau = \frac{\lambda}{v_{avg}} \tag{14}$$

where λ is the mean free path and v_{avg} is the average electron velocity. The drift velocity is therefore:

$$v_d = \frac{|q|E\lambda}{mv_{avg}} \tag{15}$$

The mean free path is proportional to temperature divided by pressure and the average velocity is proportional to temperature

$$\lambda \propto \frac{T}{P} \tag{16}$$

$$v_{avg} \propto T^{1/2} \tag{17}$$

where T is the temperature and P is the pressure. The drift velocity is therefore proportional to the electric field divided by the pressure.

$$v_d \propto \frac{E}{P} \tag{18}$$

The drift velocity is also a weak function of temperature. Since it is not a dominate term, it may be neglected for these purposes. The change in current with respect to time is:

$$\frac{\partial I}{\partial t} = A|q|v_d \frac{\partial n}{\partial t} \tag{19}$$

As previously discussed, the ion decay rate is a function of the square of pressure due to the dominant bi-molecular recombination. Assuming a constant electric field, the ion current decay rate is proportional to the pressure:

$$\frac{\partial I}{\partial t} \propto \left(\frac{1}{P}\right)\left(P^2\right) = P \tag{20}$$

From this relationship, the pressure can be determined by measuring the ion current decay rate. By using the spark plug to measure the ion current and applying this simple relationship, a complementary pressure sensing technique can be developed.

III. Experimental Approach

III.1 Chapter Overview

This chapter describes how the predicted behavior of the previous chapter will be tested. The test setup is explained along with instrumentation and data flow.

III.2 Combustion Bomb

Ultimately the spark plug is sought to be an additional pressure sensing device in the PDE. The unsteady nature of the PDE and the harsh environment make correlations between pressure and ion current difficult. Since the PDE closely follows a constant volume cycle, a combustion bomb experiment can allow investigation into the ion current dependence upon pressure. Conventional piezoelectric pressure transducers can be used in a combustion bomb with high accuracy. The correlations developed in the constant volume process can be applied to the PDE with minimal modifications.

Eventually the PDE is desired to run on practical hydrocarbon fuels. For ease of use, methane will be used as the fuel in the combustion bomb. Dry air will used for the oxidizer for both ease of use and close approximation to PDE operating conditions. While the chemistry of methane-air reactions can vary from hydrocarbon-air combinations, the methane-air mixture allows an easy first investigation.

The laminar methane-air flame speed within the combustion bomb is approximately three orders of magnitude slower than the detonation wave as previously

discussed. The laminar flame speed allows sharper time resolution into the process without expensive high speed instrumentation needed for a detonation wave.

This experiment is designed around a one half liter stainless steel pressure vessel rated to 2000 pounds per square inch (psi) as shown in Figure 2.

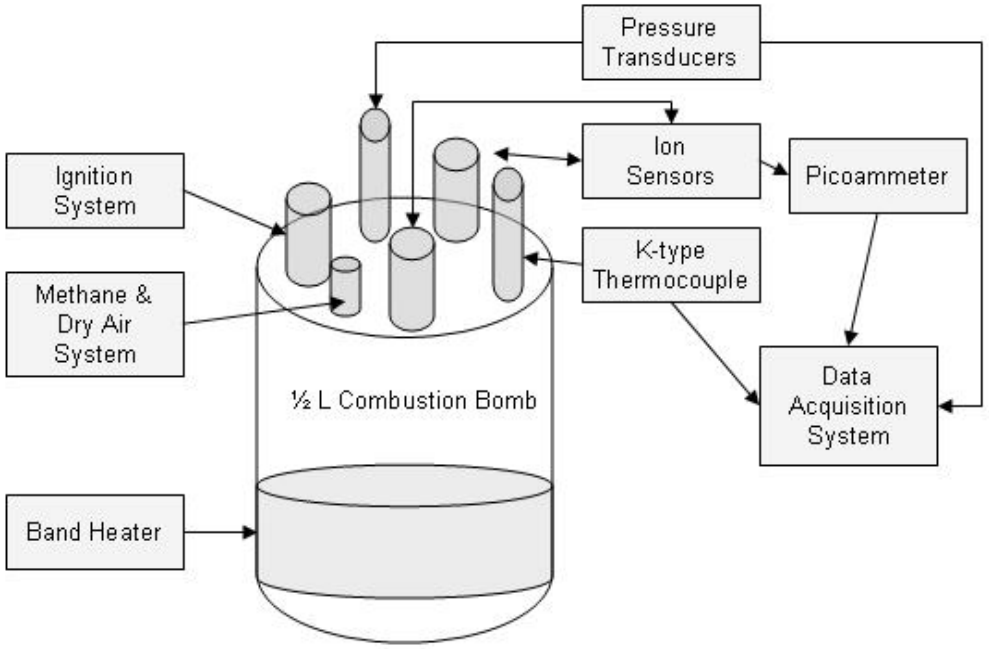

Figure 2. Overview of Experiment Configuration

A stainless steel lid with six access ports seals the 7.62 cm (3 in.) outer diameter (OD) pressure vessel. Three of the ports are 1.429 centimeters (cm) or 9/16th inch (in.) in diameter while the other three symmetric ports are 1.111 cm (7/16th in.) in diameter. A grounding point is located in the center of the lid. The depth of all of the ports is 3.175 cm (1.25 in.).

III.3 Ion Sensor

Three different ion sensors were created all based on a Champion RC12LYC spark plug used in multiple automotive engines as shown in Figure 3. The plug has a measured resistance of approximately 57.5 kΩ. This spark plug was selected because of the low cost and long center electrode. The Champion spark plug also had a compression washer needed for a tight seal against the un-tapered top of the vessel lid.

Figure 3. Champion RC12LYC Spark Plug

III.2.1 Short Probe

The first ion sensor, referred to as the short probe, simply had the side prong removed so only the center electrode was exposed as shown in Figure 4.

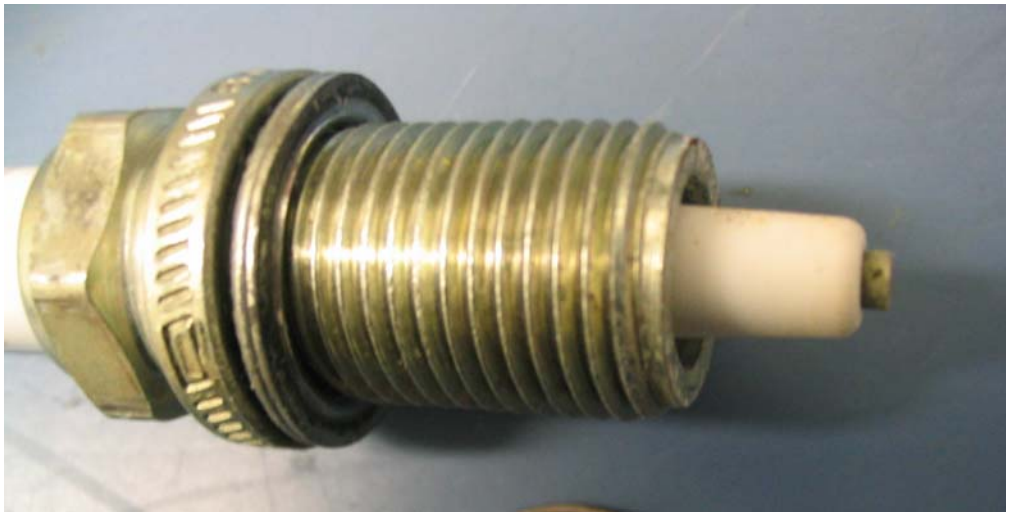

Figure 4. Short Probe with side prong of RC12LYC spark plug removed

This allowed electrons more direct access to the center electrode thereby increasing the strength of the ion current. The 0.257 cm diameter center electrode is 0.884 cm long with the bottom 0.122 cm exposed and the upper portion covered with a 0.762 cm diameter insulating ceramic material originally part of the spark plug. When placed in a port in the lid of the vessel, the bottom tip was recessed in to the threaded port by 0.57 cm. Centered in the port, the side of electrode is 0.47 cm inch from the threaded wall of the port.

III.3.2 Medium Probe

The second ion sensor, referred to as the medium probe, also had the side prong removed but the center electrode was extended to 2.54 cm (1.0 in.) as shown in Figure 5.

Figure 5. Medium Probe with 2.54 cm center electrode

This extension was created by removing some of the original ceramic material and connecting the original center electrode to a 2.54 cm (1 in.) steel extension using a 0.635 cm (0.25 in.) OD steel covering with a small set screw. The electrode extension had a diameter of 0.267 cm, similar to the original electrode with a 0.257 cm diameter. When placed into the lid, the tip of the medium probe extended 1.524 cm below the bottom surface of the lid and 1.27 cm from the vessel side wall.

III.4.3 Long Probe

The third ion sensor, referred to as the long probe, also had the side prong removed but the center electrode was extended by 10.16 cm (4.0 in.) as shown in Figure 6.

Figure 6. Long Probe with 10.16 cm insulated extension

A 0.3175 cm (0.125 in.) inner diameter, 0.635 cm (0.25 in.) OD insulating ceramic tube was placed over the extending electrode leaving 0.635 cm (0.25 in.) of the probe exposed. A larger 1.08 cm OD, 0.80 cm ID ceramic tube covered the connecting section of the electrode. Both ceramic tubes have a high electrical resistance and were secured to the electrode using blue RTV silicon designed for automotive applications. Ultra high temperature RTV was not used because of the conducting properties of the copper additive. When placed into the vessel lid the tip of the electrode extended 9.83 cm below the lid. This location of the tip also corresponds to a distance of approximately 5.0 cm from the bottom of the vessel and approximately 1.27 cm from the vessel side wall. The distance from the side of the vessel may vary slightly since the extension was not attached perfectly straight. The distance from the tip to the wall could vary by 0.12 cm depending on the final rotation of the probe into the lid.

III.4 Fuel and Air System

Both the methane and the dry air entered the vessel through one small port in the lid. This port also acted as the exit port for the combusted products. Plumbing for the dry air and methane was accomplished using 0.635 cm (0.25 in.) soft copper tubing rated to

225 psi. Brass Swagelok provided easy and reliable connections for the copper tubing. The brass valves were rated to 3000 psi. A block diagram of the air and methane fuel system is shown in Figure 7.

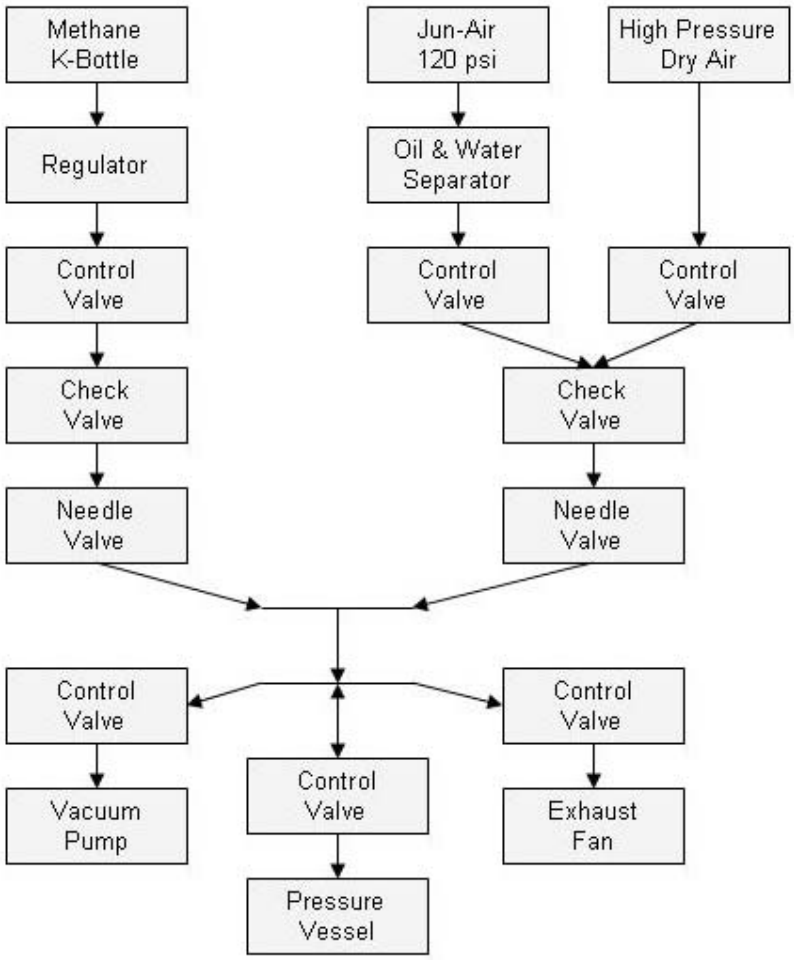

Figure 7. Fuel and air system block diagram

III.4.1 Methane

The source of methane was a commercial grade standard K-bottle mounted to the lab table. The pressure of the methane was initially controlled by a regulator on the bottle. The regulator was then connected to another valve using copper tubing. A check valve then ensured proper flow of the methane and eliminated any backflow concerns. A needle valve then tightly controlled the pressure of the methane. Before the methane entered the vessel, another shut-off valve allowed the mixture within the combustion bomb to be closed off from the other plumbing.

III.4.2 Dry Air

Two separate sources of dry air were available for the experiment also shown in Figure 7. A Jun-Air model 3-1.5 air compressor provided a 120 psi source of air. A water and oil separator attached to the compressor ensured low levels of humidity and contaminants although exact levels were not measured. A second 600 psi source of dry air was brought into the lab from an outside tank. This second source allowed for test cases above 8 atm although not required. Both sources of dry air connected to valves and then to a T connector. Similar to the methane source, a check valve and needle valve properly controlled the direction and pressure of the dry air entering the pressure vessel.

III.4.3 Vacuum Pump

A Franklin Electric 0.5 horsepower vacuum pump was connected to the vessel after the control valve with plastic tubing since high pressures would not be seen by the pump.

III.4.4 Exhaust

The combustion products were removed from the vessel through plastic tubing leading to an exhaust fan, dumping the products outside the building.

III.4.5 Partial Pressure Control

The method of partial pressures ensured accurate control of the equivalence ratio. When filling the vessel with methane and dry air the vessel pressure was measured by an Endevco 15 psi absolute (psia) conventional pressure transducer. The calibrated accuracy of the sensor was 1%. A separate Endevco 4428A conditioning box powered the sensor and controlled the calibration. The sensor was connected to the vessel through a small port that was split by a T connector. On one side of the "T" was the main pressure transducer used during the experiment to correlate the ion current. On the other side of the "T" was the Endevco transducer separated by a shut-off valve. When filling the vessel, this valve was open to allow the Endevco sensor to accurately measure the partial pressures. During the experiment and any other times where pressures were above 15 psia, this valve was closed to prevent any damage to the sensor.

The Endevco pressure transducer also aided with the vacuum pump. The sensor ensured consist vacuum levels prior to introducing the methane and dry air. The exact vacuum level the pump was capable of was unknown, but the accuracy of the Endevco sensor ensured a vacuum level of 0.15 psia or lower.

III.4.6 Fuel & Air Procedure

The vessel was first pumped down to an assumed level of 0.15 psia. Methane introduced to the system increased the pressure until the desired methane partial pressure was achieved. Once the methane flow stopped, dry air was added to the vessel to the desired total pressure. If the desired total pressure was 14.7 psia or 1 atmosphere (atm), the Endevco sensor was used to measure the vacuum level, pressure while adding methane, and the pressure while adding dry air. If the desired total pressure was above 1 atm, the valve before the Endevco sensor was closed after the methane was added. The dry air was then added and controlled using the main experiment pressure transducer. After the individual test completed, the products were sucked out the exhaust fan. The system was then flushed with dry air three times to help remove any contaminants. The vacuum pump then removed any remaining contaminants and procedure was repeated for additional tests.

III.5 Ignition System

The fuel and air mixture is ignited using a traditional automotive inductive discharge. An unmodified Champion RC12LYC spark plug, as shown in Figure 3, produces the ignition spark. A MSD Blaster 3 (MSD-8223) ignition coil generates a maximum 45,000 volts to the spark plug. This coil uses a tall tower to improve the spark isolation and coil wire attachment. The recommended 0.8 Ω ballast resistor was connected in between the ignition coil and the power supply. An HP 6033A power supply creates a clean high current 12 V DC supply for the ignition coil. The 6033A has a RMS noise level of 3 milli-Volts (mV). Typical 12 V automotive power supplies and battery

chargers easily provide the required power for the ignition but also generate unacceptable noise in the system. This occurs because the ignition spark plug and the ion probe share the common and ground signals. The ignition coil amplifies any noise in the 12 V supply. A low noise power supply such as the HP 6033A is critical to reducing overall system noise.

The electrical ignition circuit is the same as in older automotive applications as shown in Figure 8.

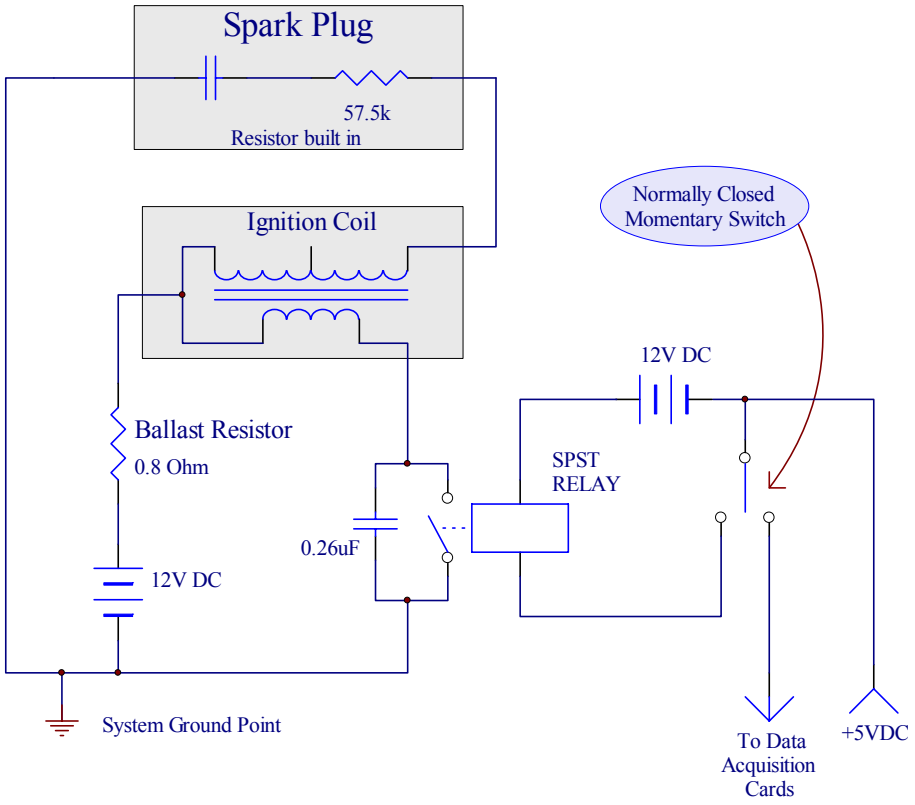

Figure 8. Ignition Circuit

The 12 V DC flows through the ballast resistor and then the coil, generating a strong magnetic field. The current then flows through a mechanical 40 Amp rated relay to the power supply common and ground. The position of the relay was controlled by a normally closed single pole double throw momentary switch. The 12 V DC powered relay was normally closed until the momentary switch was pressed causing the relay to break the ignition circuit forcing the high voltage discharge. The relay was better suited than the switch to break the circuit because of the quick break of the connection and higher durability. The swift break of the circuit is crucial to generating a strong spark across the spark plug. When the circuit is broken by the relay, the strong magnetic field induces a high voltage discharge through the secondary windings of the coil. An automotive 0.26 micro-farad capacitor was connected in parallel to the relay and ground. This capacitor forces the potential at both sides of the relay to remain at ground potential also contributing to a clean break of the circuit. Without the capacitor at the relay, the coil will not produce the required high voltage. The high voltage across the spark plug causes the mixture to breakdown into plasma creating a short but high energy region that forces ignition in the rest of the fuel-air mixture.

III.6 Instrumentation

In order to investigate the relationship between the ion current and the pressure several sensors are required.

III.6.1 DC Voltage for Ion Probes

The ion probes, as previously described, capture the ionization levels through a current across the probe when energized by a DC voltage. Each probe was energized into an ion sensor by applying a positive 10V DC from a ME 83B829 power supply. The voltage was held within a tolerance of 0.01 V. The positive voltage was placed on the center electrode while the pressure vessel was the common side of the signal. Other DC voltages of positive 5, 20, and 40 volts were also investigated.

III.6.2 Current Measurement

A Keithley 6487 picoammeter measures the current across the probe. This picoammeter has a measuring rate of 1000 Hz. For the experiments, neither the dampening function nor the internal voltage source were used. Two different scales were manually set for testing: 20 microamps (μA) and 2 μA. The internal buffer and ability to command the unit were also not used. Instead, a high speed data acquisition card (DAC) directly captured the analog output of the meter.

Shown in Figure 9, the meter was placed in the ion probe circuit between the power supply and the probe since the meter must be in series with the desired current.

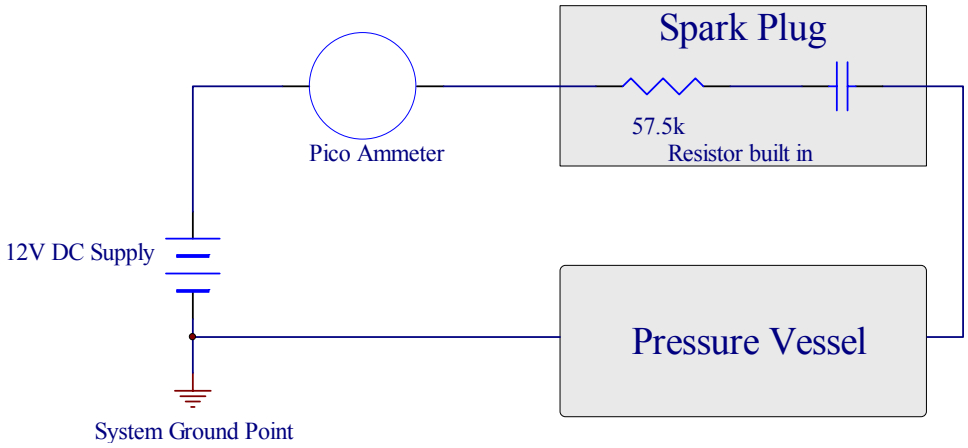

Figure 9. Ion Probe Circuit

This picoammeter also required the input high end of the device to be connected to the high resistance side of the circuit. In this case the 57.5 kΩ resistance built into the Champion RC12LYC became the high resistance portion of the circuit. Since the polarity of the power supply and the picoammeter are opposite, the current measured across the picoammeter will be displayed as negative although physically the opposite is true.

To summarize the ion probe circuit, the ME 83B829 power supply generates a small constant voltage and corresponding current. This current flows through the picoammeter and then flows across the ion probe. The common side of the probe is the thread of the spark plug that is mounted into the vessel. The ground point of the vessel is connected to a system ground point that is connected to the return side of the power supply.

III.6.3 Pressure Sensors

For pressure measurements two different Omega transducers were used depending on the maximum expected pressure in the vessel. The conventional Omega PX303-300A5V transducer measured pressures for test cases with an initial pressure of 3 atm or less. This transducer useful range is from 0 to 300 psia with a response time of 1 ms. For test cases above an initial pressure of 3 atm, a similar Omega PX303-1KG5V transducer measured pressures from 0 to 1000 psi gauge (psig). The gauge pressure readings were converted into absolute pressures by adding the atmospheric pressure in the lab as measured by a Druck DPI-141 digital barometer. While the accuracy of both transducers is the same percentage, the higher range of the 1000 psig transducer provides less resolution into the pressure. An Omega PSS-15 power supply powered the Omega transducers. Both transducers produced a 0.5-5.5 V signal corresponding to the minimum and maximum pressure respectively.

III.6.4 Thermocouples

Two K-type thermocouples were used in the experiment to measure the ambient temperature in the lab and the internal temperature of the combustion bomb. The ambient sensor was directly connected to a SCXI-1112 signal conditioning module described later in this chapter. The internal thermocouple was inserted into the vessel through one of the small ports in the lid and secured with a graphite compression fitting. The tip of the thermocouple extended approximately 0.32 cm below the bottom surface of the lid. This position was selected to measure gas temperature without interfering with other sensors.

III.6.5 Band Heater

A Chromalox band heater, located at the bottom the pressure vessel, increases the temperature of the gases in the lower portion of the vessel. Due to the generated buoyancy, the dense gases rise towards the top of the vessel where the cooler temperatures allow density to increase causing the gas to drop back towards the bottom. This buoyancy increases the mixing of the lighter methane with the denser dry air. In addition to the buoyancy effect, the band heater also raises the overall temperature of the pressure vessel. The band heater is controlled by an Omega CSC32 bench top controller that allows the temperature to be manually set or remotely through a computer program using the serial port. The controller measures the temperature of a thermocouple inserted in between the pressure vessel and the band heater. This indicted the temperature of the band heater and not the internal temperature of the gases in the vessel nor the ambient temperature.

The 120 V AC powered resistance band heater operated intermittently. A proportional-integral-derivative (PID) controller maintained the set temperature for the heater. The controller was tuned using the software included with the controller. Using this controller, the temperature of the band heater stayed within 2 ˚C of the set point at all times. In addition to displaying the current temperature, the PID controller also indicted when current flowed through the resistance heater.

III.7 Data Flow

The data from the sensors traveled through one of two routes as indicted in Figure 10.

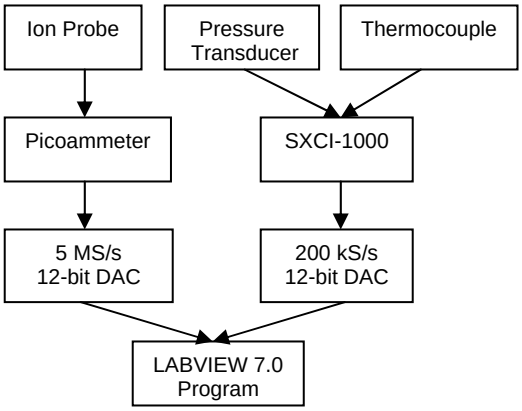

Figure 10. Experiment Data Flow

The picoammeter measured the ion current and sent the results to a high speed DAC where a LabView program captured the data. The pressure sensors and thermocouples used a SCXI-1000 chassis to pass the data before being read by a slower DAC again where a LabView program captured the data. The data was then plotted and analyzed using MatLab.

III.7.1 SCXI-1000 Chassis

The National Instruments (NI) SCXI-1000 chassis provides an easily configurable platform to pass, condition, and multiplex input and output signals. The chassis has space for up to four modules although only three were used for this experiment. A SCXI-1112 module was used to amplify and condition both the internal and ambient thermocouple signals. A SCXI-1180 module provided a direct pass through of signals straight to the DAC. A SCXI-1302 breakout box connected to the SCXI-1180 module allowed simple

hookups to the 50 pin feed-through panel. The signals from the Omega pressure transducers were connected to the SCXI-1302 breakout box since no conditioning of the signal was required. The previously described double throw ignition switch used one throw to break the ignition circuit causing the high voltage discharge. The other throw on the switch changed a normally 0 V signal to a +5 V DC signal that was read by both the slow and fast DACs. This timing signal triggered the data capture of the combustion event. A third SCXI-1124 digital to analog converter module with a SCXI-1325 breakout box provided analog out signals to control other hardware. The speed of SCXI-1000 chassis has a maximum 200 kilo-Samples per second (kS/s) for all channels. The signals routed through the SCXI-1302 module were not part of the SCXI-1000 sample rate but rather the rate of the DAC card itself. In this configuration the SCXI-1000 required an E-series NI DAC.

III.7.2 NI 6024E DAC

A NI 6024E DAC provided data capture for up to eight 12-bit channels at 200 kS/s. This NI E-series card was able to use the updated LabView mx drivers in addition to the traditional LabView drivers. This card, however, does not support hardware triggering. This slower DAC card captured the pressure and thermocouple data. The +5 V ignition timing signal was also captured by this card. The card also read the multiplexed signal from the SCXI-1000 chassis.

III.7.3 NI 6110 DAC

A NI 6110 DAC supplied data capture on four 12-bit channels of up to 5 mega-samples per second (MS/s) per channel. While this fast data capture rate was excessive for this experiment, the extra speed could be useful for testing in the PDE itself. This card was not supported by the new LabView mx drivers but was capable of hardware triggering. The ion current was captured by one channel of this device while another channel was used to capture the +5 V ignition timing signal. This card does not support a SCXI-1000 chassis.

III.7.4 Labview Program

The LabView 7.0 software package was used to control experiment conditions, capture sensor data, and display results. LabView operated under Windows 2000 Professional on a computer with a 1000 MHz Pentium processor and 256 MB of memory.

III.7.4.1 Program Modes

A LabView Virtual Instrument (VI), or program code, was written to operate in two different modes. The first mode continuously displayed sensor data onto the computer screen allowing quick checks of system operation and proper initial conditions before initiating the experiment. Once all conditions were satisfactory, the program was manually changed to the data acquisition mode. Under this mode the LabView program began searching the incoming data for the ignition timing signal. Once the timing signal changed from 0 to +5 V, the data acquisition began. Data 0.1s before and 1 s after this

trigger were transferred from the DACs internal buffer and into the main system memory. Any data in the buffers before or after this period was discarded. With the useful information in memory, the data was formatted and saved into two separate data files, one for each DAC.

III.7.4.2 DAC Drivers

Since only the E-series card was supported by the new LabView mx drivers, the main VI had to be written using the older traditional VIs and routines. This complicated the program since easier improved tasks in the new mx driver could not be used. Despite this obstacle, the main VI worked well once bugs in the program were worked out.

III.7.4.3 Triggers

The lack of a hardware trigger on the E-series card also complicated the programming. The fast 5 MS/s/channel DAC provided hardware trigger capability where the card itself searched the incoming data for the required trigger value. In this way, hardware triggering uses minimal computer system resources and is time accurate within half the sample time. To overcome this deficiency with the E-series card, a software conditional trigger scheme was applied. This scheme transfers the data from the internal buffer on the slow DAC into system memory where the LabView program searches the data for the desired trigger value. This conditional software trigger can take considerable processing power and system memory depending of the data rate. Since only the slow DAC used this scheme, the burden of the computer did not reduce the functionality of the rest of the LabView program. In other words, the computer was still powerful enough to

complete the other required LabView tasks at the same time without impacting results. Another disadvantage to the conditional trigger was the lower time accuracy. When transferring the data from the internal buffer to the system memory there is a greater chance for skewing of the measurement time. The times between samples remains constant but some error could be introduced that varies the triggering time. Both triggers, despite reading the same timing signal at the same trigger level, could have slightly different start times. Although not desirable, this timing error was acceptable for this experiment.

III.7.5 Acquisition Rates

Acquisition rates of both DACs were selected to make the instruments the limiting factor in the data rate and not the cards themselves. A rate of 10 kS/s/channel was selected for the slow E-series DAC. This rate was easily fast enough to capture the pressure and temperature and provided good time resolution into the timing signal without overburdening the computer. A rate of 100 kS/s/channel was selected for the fast 6110 card. This speed easily captured the ion current signal from the picoammeter without creating excessive amounts of data. As previously described, the data was acquired for a total of 1.1 s with 0.1 s of data before the trigger.

III.8 Shielding

Initial tests conducted to work out the bugs in the system showed high levels of noise in the ion current. Some noise was expected due to the low micro-amp currents being measured. The ion current signal was analyzed in LabView by using a built-in fast

Fourier transform (FFT) and then plotted the results against the frequency. This revealed a spike in the signal at 60 Hz. This noise was assumed to be generated from a combination of a poor facility ground, fluorescent lighting, various power supplies, measurement instrument themselves, and the nearby computer. Moving the setup to a lower noise electronics lab was not possible due the hazardous methane. Instead, the noise was reduced by creating a better single point system ground and improving shielding on signal wires. The signal wires already had standard wire insulation and in some cases such as the picoammeter cable, a shield protected portions of the wiring. Aluminum tape was wrapped around the unshielded wires and then connected to the appropriate ground point. By adding the shielding, the 60 Hz was reduced by over 10 dB but still remained the dominate source of noise as expected. While noise is not desirable, the ion sensor will also experience noise when employed in the PDE. The more noise the sensor is able to handle in the laboratory setting the easier it will be to successful employ the sensor in the PDE.

III.9 Steady State Ion Current Experiment

Initially, the steady state ion currents were desired to be a useful comparison against levels measured during and after combustion. This first experiment used a Glassman model PS/FC20R06.0-11 high voltage power supply capable of up to 20,000 volts positive or negative. This power supply was remotely controlled using the LabView program with the control signals being sent through the SCXI-1124 module. The actual voltage and current supplied were read into the LabView program through the SCXI-1302 module and collected by the slow DAC. The high voltage was placed on the long

probe making it an ion generator. The voltages selected for each pressure were slightly lower than the required voltage for the probe to arc to the wall of the pressure vessel. Ion levels were then measured across the medium probe using the picoammeter. For a variety of pressures, the ion current was examined. Unfortunately, the extremely low currents generated by this method were not detectable by the picoammeter. Either the current was too low or the surrounding noise in the system masked any measurable current not due to the electric field. Since this investigation was not critical to the overall understanding of the ion sensor, this part of the experiment was abandoned in favor of the following method.

III.10 Transient Ion Current Experiment

Due to the lack of results from the steady state tests, a variant of that method was conducted by investigating the unsteady case. By instantaneously removing the high voltage and thereby the dominant electric field, the remaining current would be due to the ionization of the gas and should decay according to the pressure. Again, this experiment made use of a high voltage power supply and the LabView program. By clicking on a button in the LabView, the Glassman power supply was commanded to 0.0 V and the DACs were triggered to acquire data. Even though, theoretically, the ion decay rate could be investigated in this manner the Glassman power supply could not instantaneously drop the voltage. The stored energy in the power supply drained over several seconds. The resulting change in current across the ion probe was simply due to the change in the electric field. Again, the physics of the ion decay could not be examined due to the limitations of the experimental setup. Although a different electrical circuit could have

helped alleviate the problem, ion generation levels were still expected to be difficult to measure without major experiment redesign. This method was also abandoned in favor of the combustion portion of the experiments.

III.11 Combustion Experiment

The main effort in this investigation was the combustion experiment where the ion current levels generated by the combustion of methane and dry air could be directly compared to the pressure.

III.11.1 Initial Conditions

A band heater temperature of 50 degrees Celsius (˚C) created the buoyancy needed for mixing of the methane and dry air. This band heater temperature corresponded to an internal temperature of approximately 30 ˚C. The fuel-air mixture was difficult to ignite at 1 atm at this temperature. A higher temperature of 99 ˚C increased the mixing within the vessel and eased ignition difficulties. This band heater setting corresponded to an internal temperature of 45 to 65 ˚C. Successive tests caused the heating of the vessel and increased the initial temperature despite removal and injection of new reactants. Some variation therefore occurred in the initial temperature. All tests began with the band heater setting at 99 ˚C.

III.11.2 Test Cases

The baseline case was considered the test with an initial pressure of 3 atm, equivalence ratio of 1.0, using the medium probe for the ion sensor with a +10 V DC

bias, a band heater setting of 99 ˚C, and the picoammeter scale set to 20 μA. The following test matrices were developed based on searching out from this baseline test.

Table 1. Test cases for medium probe at +10 V DC

Pressure (atm)	Equilvance Ratio (φ) 0.7	1	1.2
1	3/3	3/1	3/1
2	1/1	1/0	1/1
3	3/3	3/3	3/3
5	1/1	3/3	1/1
7		1/1	

Number of tests at High Scale/Number of tests at low scale

Table 2. Test cases for long probe at +10 V DC

Pressure (atm)	Equilvance Ratio (φ) 0.7	1	1.2
1			
2			
3	1/1	2/1	1/1
5			
7			

Number of tests at High Scale/Number of tests at low scale

Table 3. Test cases for short probe at +10 V DC

Pressure (atm)	Equilvance Ratio (φ) 0.7	1	1.2
1			
2			
3	1/1	1/1	1/1
5		1/0	
7			

Number of tests at High Scale/Number of tests at low scale

Table 4. Test cases at various voltages at 3 atm and φ = 1.0

Voltage (DC)	Probe Short	Medium	Long
5		1/1	
10	1/1	3/3	2/1
20			1/0
40		1/1	1/0

Number of tests at High Scale/Number of tests at low scale

III.11.3 Test Procedure

The procedure for running each test was as follows. The desired test case was selected and the fuel and air procedure was used to fill the vessel with the appropriate partial pressures of both methane and dry air. The power supply for the ignition circuit relay was brought to 12 V DC and the ignition power supply was raised to the required 12 V DC. After ensuring proper conditions with the continuous mode of the LabView program the mode was changed to data acquisition. After confirming the program successfully transferred modes and waiting a couple seconds, the ignition switch was pressed causing a spark that ignited the mixture. Because a small but noticeable amount of noise was generated simply by depressing the switch, the momentary switch was not released until after 1 second. This ensured any noise generated by the switch would not influence the results. The timing of the ignition also coincided with no current following through the band heater. This was accomplished by visually watching the indictor on the band heater controller. The data files were then saved to the hard drive. The combustion products were removed following the previously described procedure for the fuel and dry air.

IV. Raw Data

IV.1 Chapter Overview

This chapter describes the error in measuring the physical values and shows the raw data before any data reduction. Interesting features of the raw data are highlighted.

IV.2 Measurement Error

For each measurement the error was calculated from the accuracies of each device involved in the measurement. The time error in the current measurements was one half of the time between each sample because of the accurate timing of the hardware trigger of the fast DAC as previously discussed. The time error for the slow DAC, also as previously discussed, was not only half the sample time but included possible errors from the conditional triggers. Assuming the errors imposed by conditional trigger are negligible, the time errors were 0.1 ms and 10 μs for the pressure and current respectively.

The root of the sum of the squares (RSS) method, as described by Wheeler and Ganji [24], provided a suitable error estimate for the pressure and current measurements. The error in the pressure measurements was 0.0513 atm for initial pressures of 1atm to 3 atm and an error of 0.171 atm for initial pressures of 5 atm and 7 atm. The error in the current measurement was 2.79% for the 20 μA scale.

For each figure, error bars were added at several points to indicate the error levels, how the variations in each test compared to the error, and how the signal noise compared to the error levels.

IV.3 Results of Raw Data

The baseline case with an equivalence ratio of 1.0 and initial pressure of 3 atm was repeated 3 times as shown in Figure 11. Unless otherwise stated, each case used the medium probe energized with 10 V DC with a band heater setting of 99˚ C and a scale of 20 μA on the picoammeter. Time of 0.0 seconds corresponds to depressing the ignition switch and not the time the spark actually occurred.

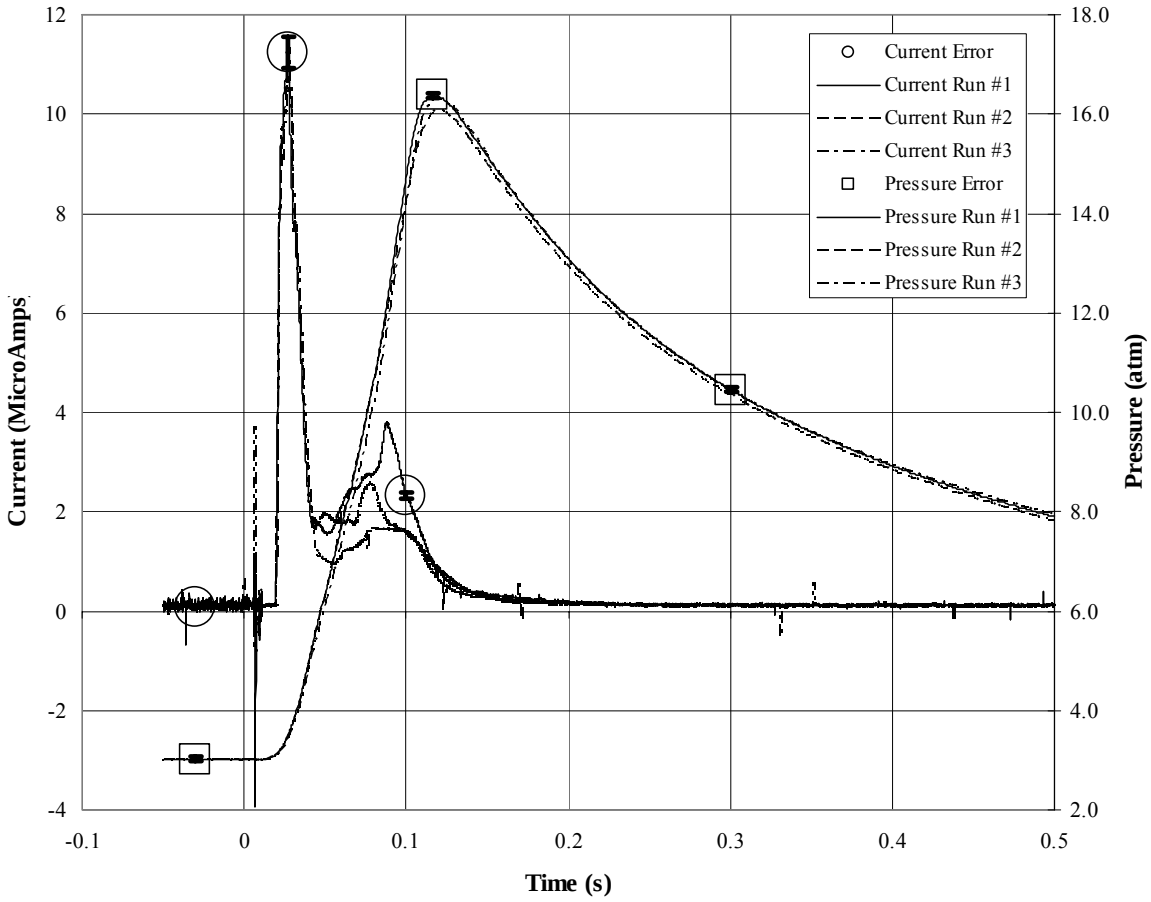

Figure 11. Runs at the baseline case of φ = 1.0 at an initial pressure of 3 atm

The large noise just after 0.0 seconds is due to interference and effects of the ignition spark. The square and circle objects are indictors of where errors were computed and not the actual size of the error. Error bars within the objects show the actual size of the error. The measurement errors in Figure 11 are difficult to discern due to their relatively small size compared to actual measurement levels. Figure 11 overall shows good repeatability of the measurements.

The impact of changing the ion probe voltage from 10 V DC to 40 V DC and 5 V DC is shown in Figure 12.

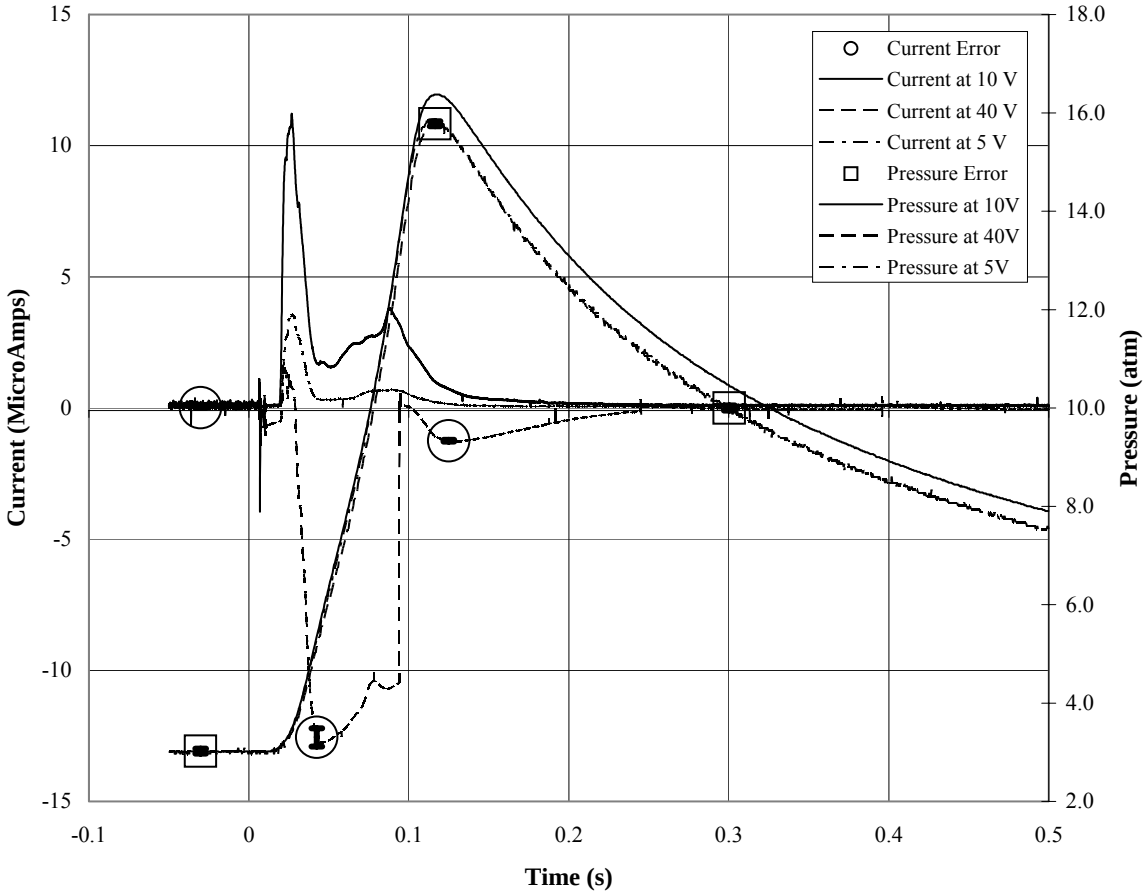

Figure 12. Comparison of 5V, 10V, & 40V across the ion probe at an initial pressure of 3 atm and $\varphi = 1.0$

The 5V case shows reduced current levels but similar trends to the 10V case. The polarity of the current switches in the 40V case and the signal appears to become saturated. Again, error bars are shown at select points for comparison purposes.

At an initial pressure of 1 atm, the effects of changing the equivalence ratio are shown in Figure 13.

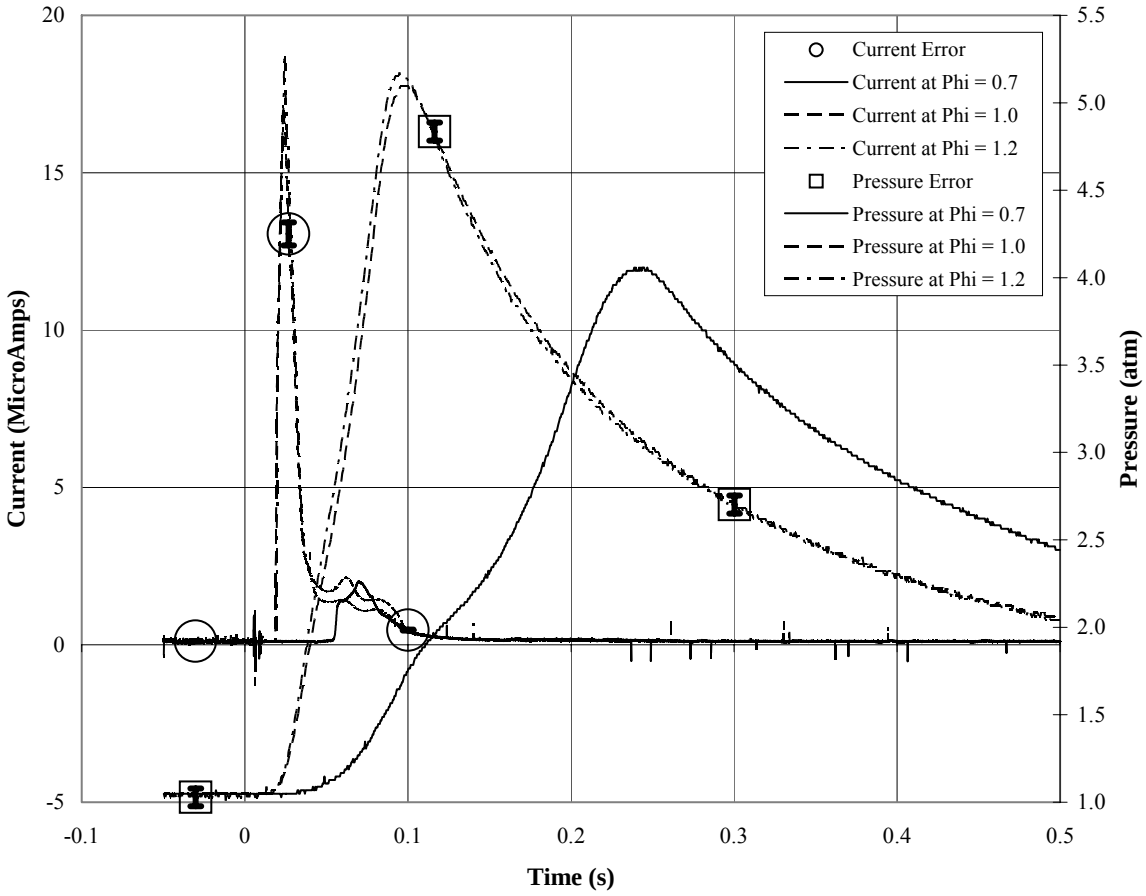

Figure 13. Effects of φ = 0.7, 1.0, & 1.2 at initial pressure of 1 atm

Both the φ = 1.0 and 1.2 cases show similar measurement levels and trends. The φ = 0.7 case shows a time delay in the pressure peak and lower peak level. The current in this case does not display a sharp spike but a low peak of approximately 2 μA.

At an initial pressure of 3 atm, the effects of changing the equivalence ratio are shown in Figure 14.

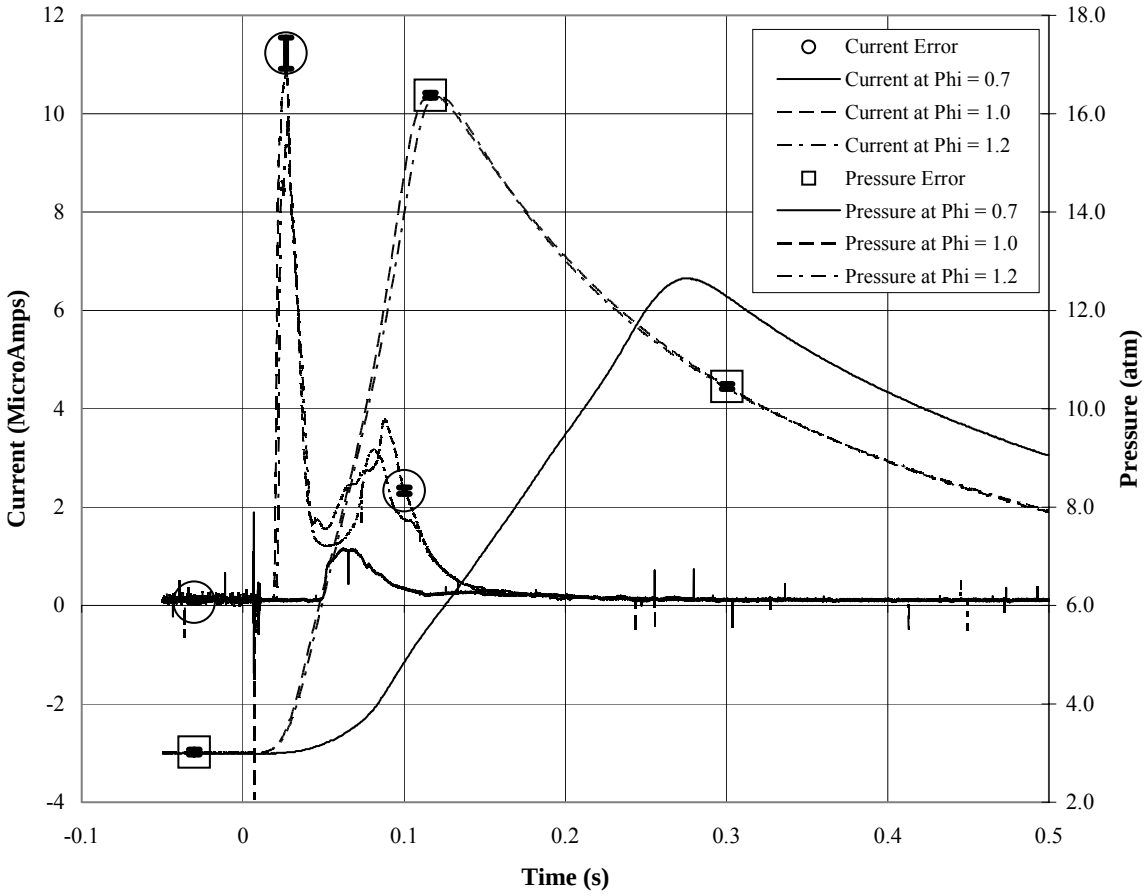

Figure 14. Effects of φ = 0.7, 1.0, & 1.2 at initial pressure of 3 atm

Again, both the φ = 1.0 and 1.2 cases show similar measurement levels and trends. The φ = 0.7 case shows a time delay in the pressure peak and lower peak level. The current in this case does not display a sharp spike but a low peak of approximately 1 μA.

At an initial pressure of 3 atm, the effects of changing the equivalence ratio are shown in Figure 15.

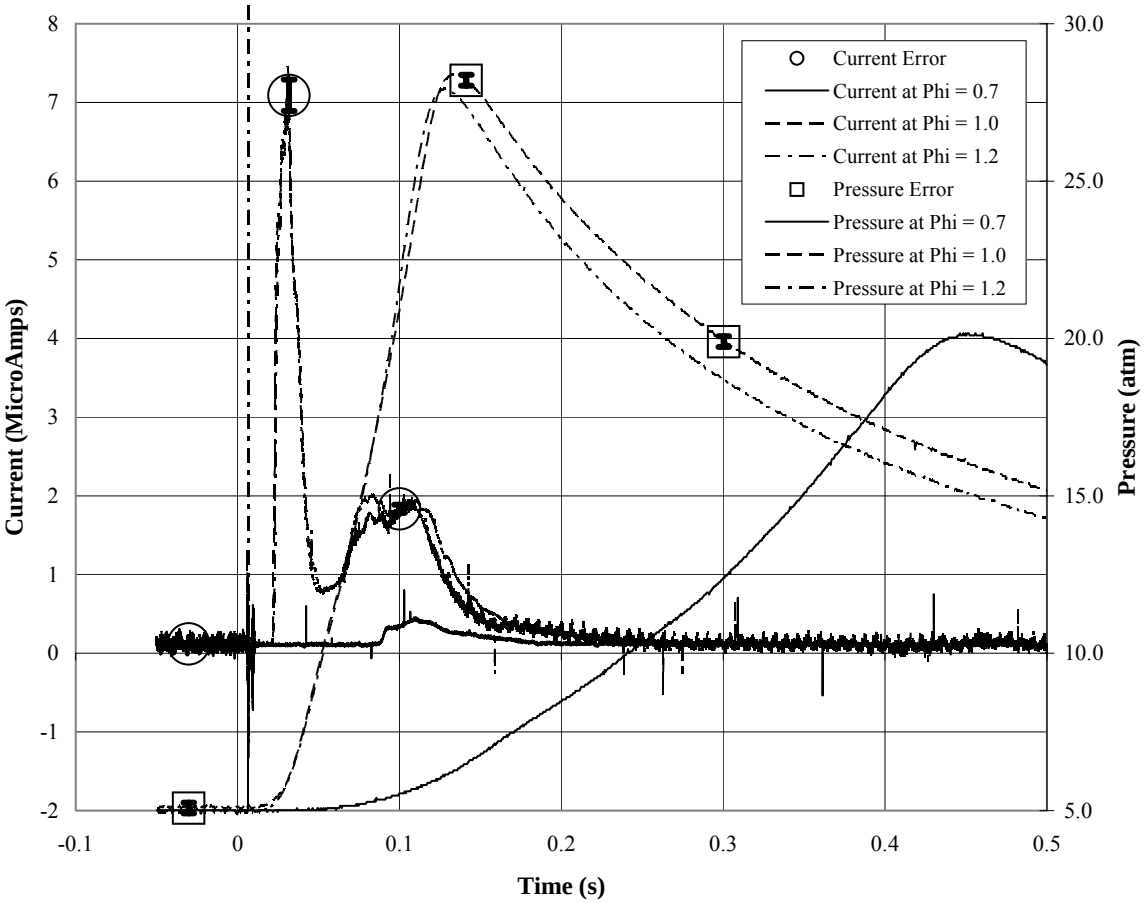

Figure 15. Effects of φ = 0.7, 1.0, & 1.2 at initial pressure of 5 atm

As previously shown in Figures 3 and 4, the φ = 1.0 and 1.2 cases show similar measurement levels and trends. The φ = 0.7 case shows a time delay in the pressure peak and lower peak level. The current is this case does not display a sharp spike but a low peak of approximately 0.5 μA.

The changes in pressure and ion current for initial pressures of 1, 3, & 5 atms are shown in Figure 16.

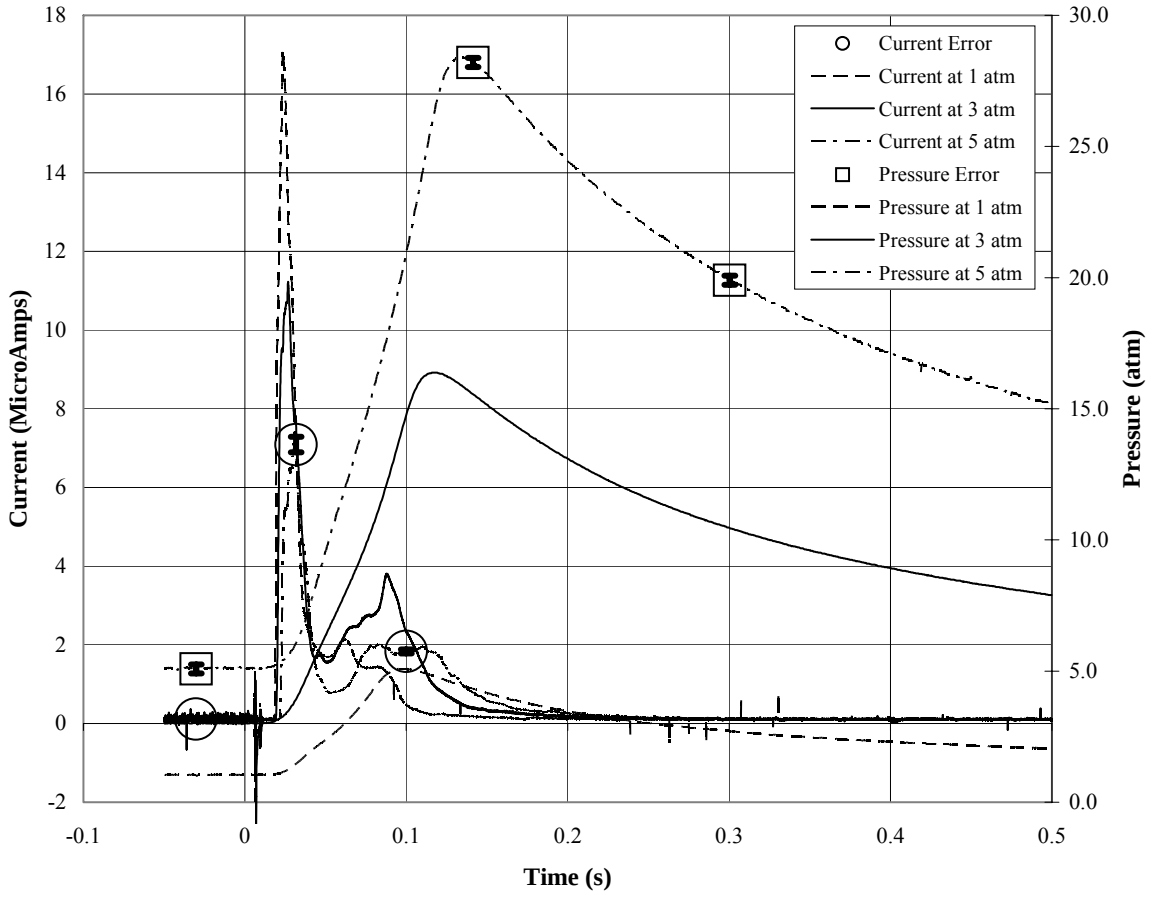

Figure 16. Effect of initial pressures of 1, 3, & 5 atm at $\varphi = 1.0$

As seen in Figure 6, increasing initial pressure results in lower ion current peaks. The trends of the ion current and instantaneous pressure for each initial pressure are similar however the timing of the pressure peak shows a slight time delay at higher initial pressures.

The area of interest in Figure 6 is expanded and more clearly shown in Figure 17.

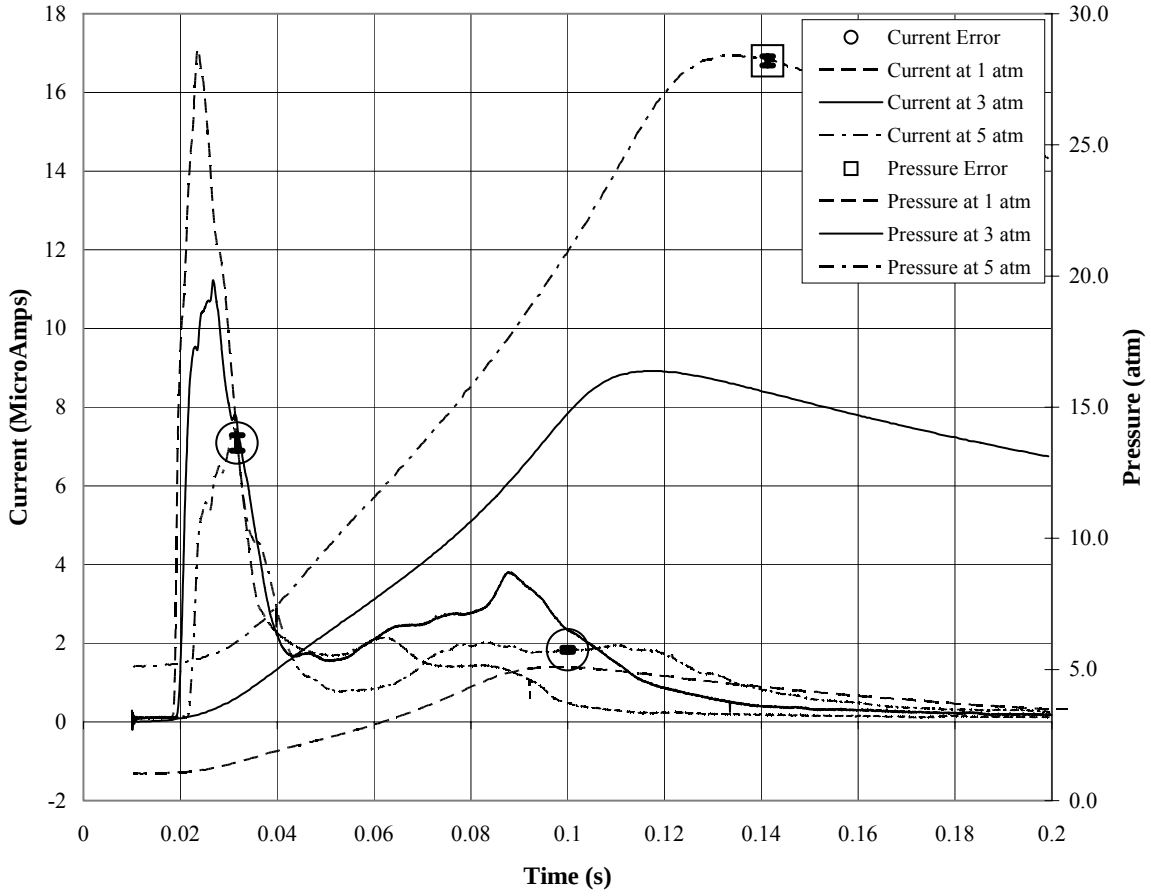

Figure 17. Zoomed in view of Figure 16, effects of initial pressure of 1, 3, & 5 atm at $\varphi = 1.0$

In Figure 17, the ion current also shows a slight time delay for higher pressures.

The effects of changing the probe length for the baseline case of 3 atm at $\varphi = 1.0$ are shown in Figure 18.

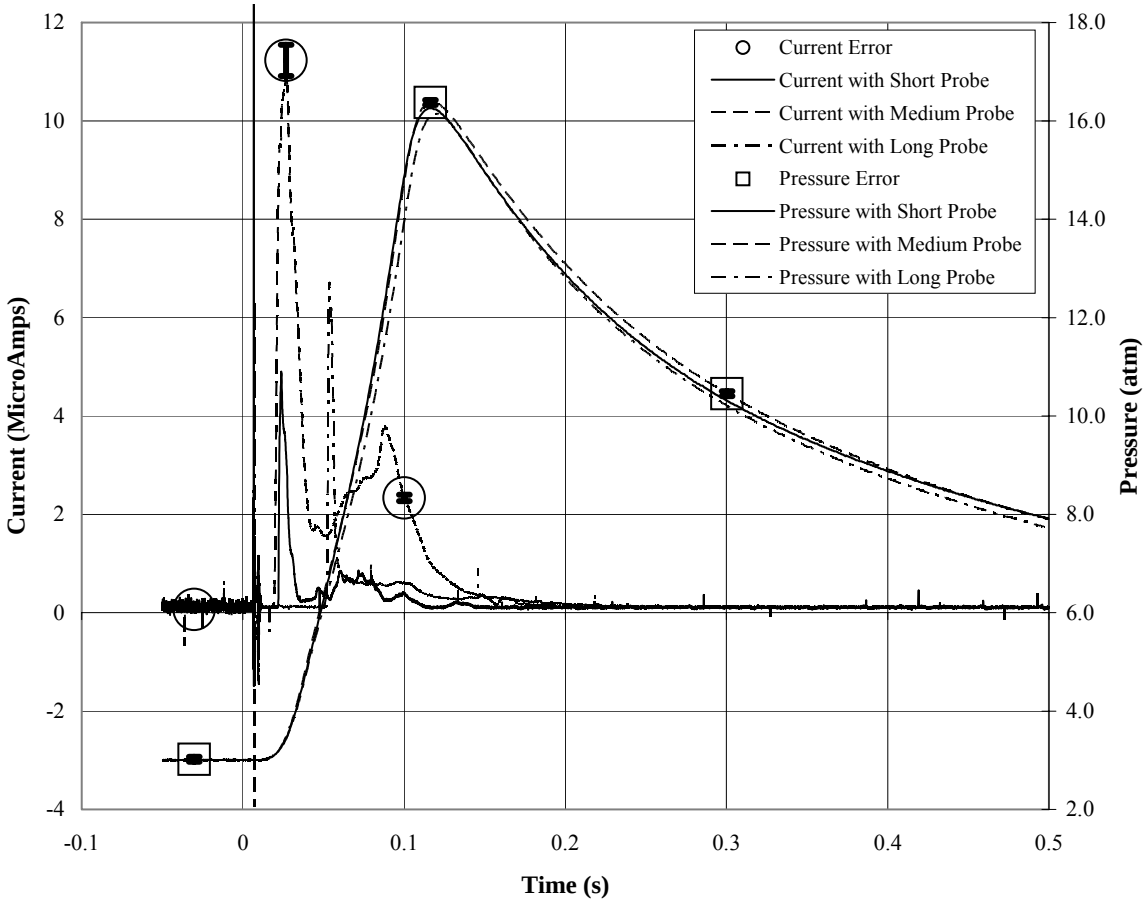

Figure 18. Effects of probe length at baseline case of φ = 1.0 at 3 atm

The large narrow spike near 0.0 seconds was due to the interference of the ignition spark. The baseline medium probe produced the highest ion current peak followed by the long probe with the short probe producing the smallest ion current peak. The short probe current peak had a slight time delay compared to the medium probe due to the further distance from the ignition spark. Likewise, the long probe showed a greater time delay since the 10 cm extension placed it even further away from the source of the ignition.

Figure 19 shows an exploded view of the features of interest in Figure 18.

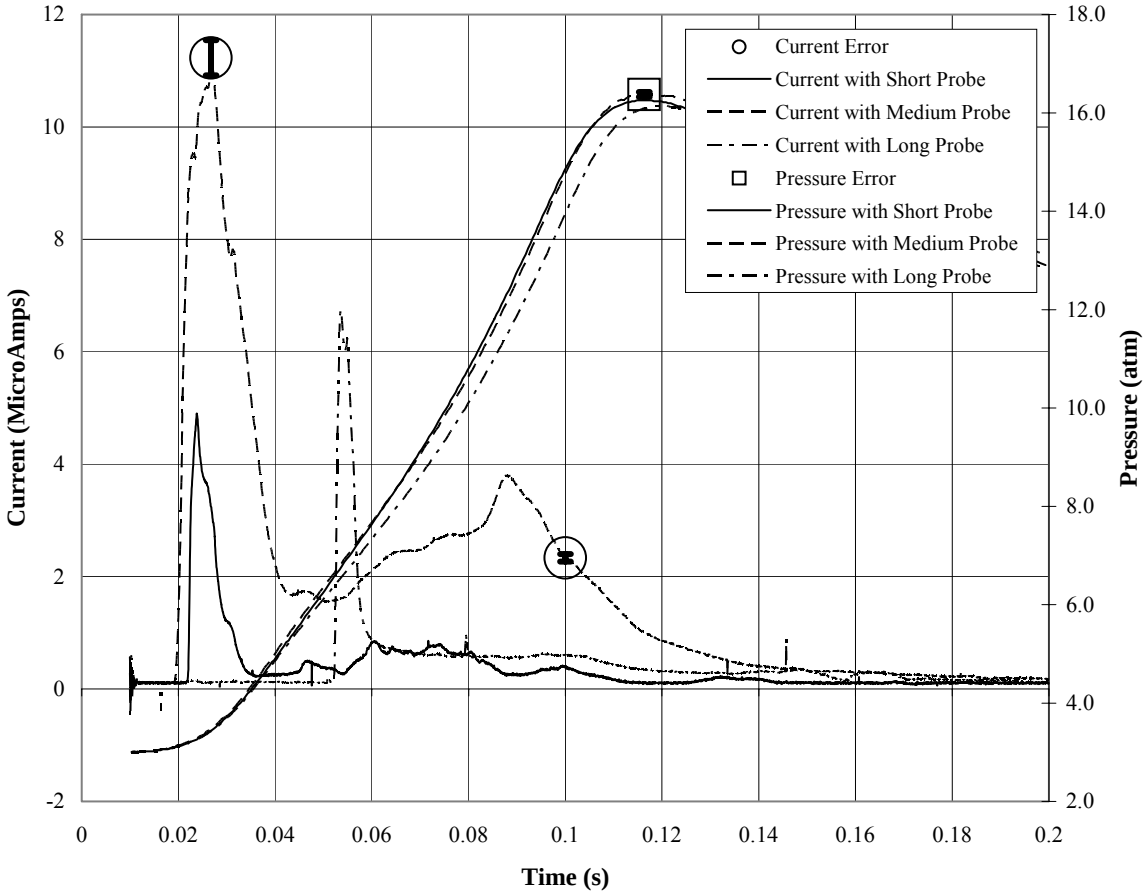

Figure 19. Zoomed in view of Figure 18 more clearly showing the effects of probe length at the baseline case of φ = 1.0 at 3 atm

The pressure measurements in Figure 9 show relatively small variations while the ion current peak shows large differences in both peak level and peak timing. In Figure 19, the time delay between the ion current peaks is more clearly evident.

V. Data Reduction and Discussion

V.1 Chapter Overview

In this chapter the data is analyzed and compared against predictions of Chapter II. Features of the raw data are examined and compared against expectations. The data is then reduced by several methods including averaging the results over similar cases, computing the derivative of the ion current signal, and filtering out noise. Features of the reduced data are also examined and compared against expectations.

V.2 Analysis of Raw Data

The ion current from the raw data shown in Chapter IV displays initial noise due to the ignition spark, a sharp peak a short time later due to the chemi-ionization as the flame front passes the probe, and a smaller secondary peak after the sharp peak. The strength of the secondary peak is highest for the 3 atm case as shown in Figure 16. When compared to the sharp chemi-ionization spike, the shape and strength of the secondary peak is irregular even for repeated cases as shown in Figure 11. This secondary peak could be the result of NO production similar to the IC engines. Since both temperature and pressure are much lower than in IC engines, the NO would not be the dominant source of ionization in the secondary peak. Non-uniformities and a three dimensional flame front are more likely the cause of the secondary peaks. Due to the surface area of the medium probe, the flame front may pass near the sensor multiple times producing

additional ionization. The variability and structure may provide useful information for PDE but that investigation is beyond the scope of this thesis.

Equivalence ratios of 1.0 and 1.2 show similar signal levels and trends. The 0.7 equivalence ratio, however, shows little resemblance to the other two ratios. The pressure peak is significantly lower and the ion current spike, the dominant feature of the other two ratios, is nonexistent. This trend of lower ion currents with low equivalence ratios is expected. Equation (1) implies the ionization production strongly depends upon the concentration of the fuel. Further, the recombination of ions, as shown in Eq (5), strongly depends upon the oxygen concentration. The complete absence of the spike, although not expected, agrees with the trend of lower ion currents at lower equivalence ratios. In addition, the only peak in the 0.7 equivalence ratio cases correspond, although a lower level, to the secondary peaks shown in cases of 1.0 and 1.2 equivalence ratio. This also agrees with the expected trend.

Since the Omega pressure transducer had a stand off distance of approximately 10 cm from the lid of the pressure vessel, this could impact the pressure measurements. Any stand off distance would influence the measurements by smoothing any pressure spikes in the vessel. Because of the deflagration in the constant volume process, pressure spikes are not expected. The PDE, however, does have the von Neumann pressure spike as previously described by the ZND wave structure. For the purposes of this experiment any smoothing of the pressure measurement is considered negligible. The stand off distance still can introduce a time delay in the pressure signal. At an approximate initial gas temperature of 50 ˚C, the mixture has a speed of sound of roughly 360 m/s. A stand-off

distance of 10 cm therefore results in a time delay about 0.028 ms. This small delay also can be considered negligible.

V.3 Error Analysis

In addition to the measurement errors calculated in Chapter IV, the error of the equivalence ratio was also computed using the RSS method. The resulting error for each initial pressure and equivalence ratio is shown in Table 5.

Table 5. Percent Error in Equivalence Ratio

	Equivalence Ratio		
Pressure (atm)	0.7	1.0	1.2
1	11.2 %	11.9 %	12.3 %
2		5.9 %	
3	3.7 %	4.0 %	4.1 %
5	2.2 %	2.4 %	2.5 %
7		1.7 %	

The errors at 1 atm are greater due to the limited accuracy of the 15 psia Endecvo transducer for both the vacuum pressure and the partial pressure of the fuel. At higher total pressures, the relative error in the fuel partial pressure decreases.

In analyzing the ion current the derivative of the signal was calculated using a fourth order accurate scheme. The resulting error in the derivative was 3.94 % compared to 2.79 % for the ion current signal.

V.4 Reduced Data as a Function of Time

Because of the variability of the ion current, the average of three runs at one condition was calculated as shown in Figure 20.

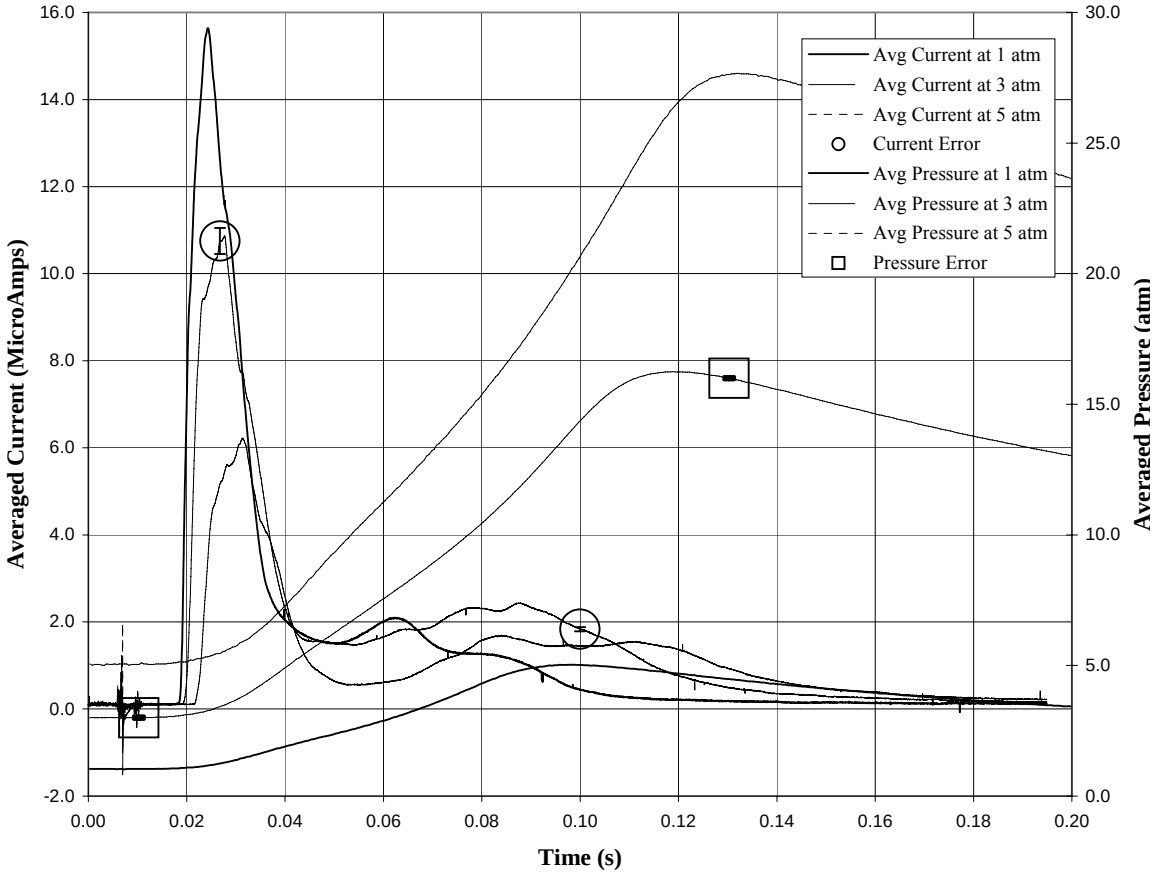

Figure 20. Averaged Current and Pressure for initial pressures of 1, 3, & 5 atm at φ =1.0

As in Chapter IV, error bars are included in Figure 20 at select points. The time scale was narrowed to allow better resolution into the current spike. Compared to the signal levels, the error in both the current and pressure measurements are relatively small. The initial noise in the ion current is due to the ignition spark. When averaged over the three runs, the time differences between the signals create a smoothing of the current spike. Despite this effect, the same trends are seen with the 1 atm case showing the strongest current spike and the 5 atm case showing the weakest current spike.

The pressure and current ratio model developed by Saitzkoff et al. was applied to the baseline test condition to evaluate the suitability of the model to these test conditions. After normalizing the measured pressure, the predicted current was plotted in Figure 21 and compared to the measured current after normalization.

The model was developed for use in IC engines where the maximum pressure and combustion occur when the piston is near the top of cylinder. The constant volume combustion process is inherently different. In the constant volume process the flame front passes the sensor well before the maximum pressure in the vessel is produced. This effect is clearly shown in Figure 21 by showing the measured current spike well before the predicted values. Based on these results, the Saitzkoff et al. model is not suitable for pressure predictions in the constant volume process.

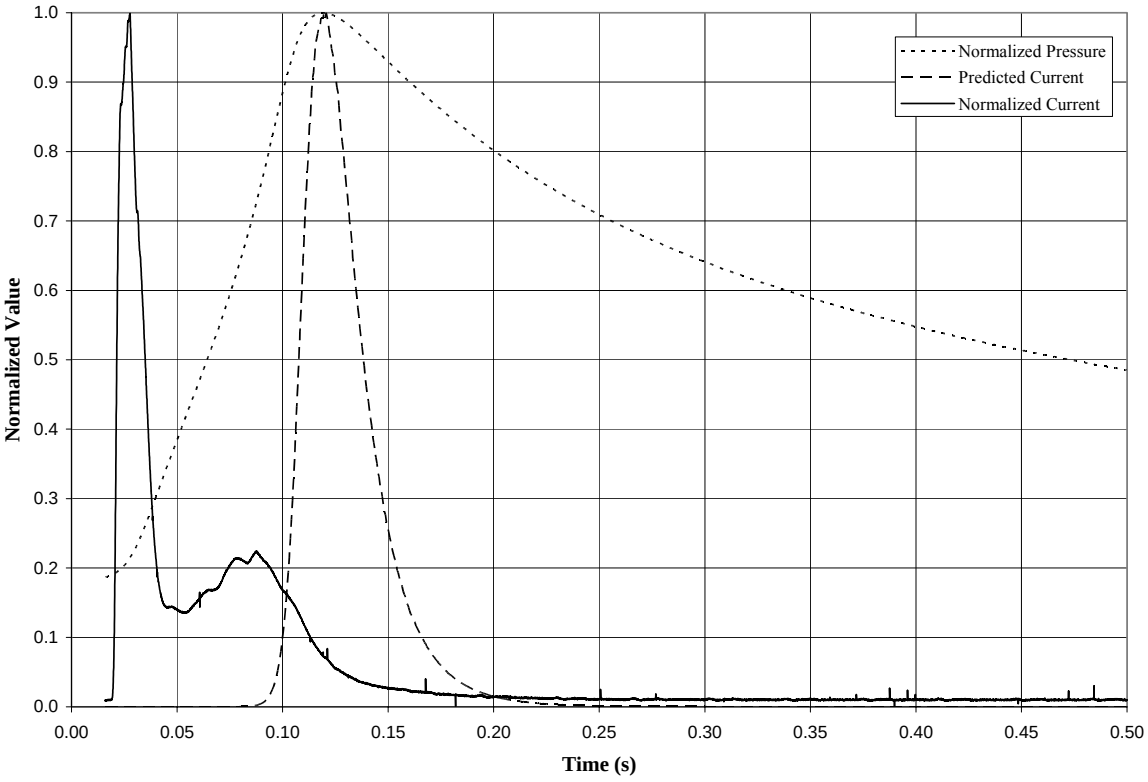

Figure 21. Saitzkoff et al. model applied to this experiment at baseline condition of 3 atm initial pressure and φ = 1.0

The rate of change or derivative of the ion current was predicted in chapter II to be a function of the pressure squared. The derivative was calculated using a 4th order accurate scheme:

$$\left\{\frac{\partial u}{\partial t}\right\}_i = \frac{-u_{i+2} + 8u_{i+1} - 8u_{i-1} + u_{i-2}}{12h} + O\left(h^4\right) \tag{21}$$

where h = Δt. and *i* is the point the about which the derivative is computed. By taking the derivative, the noise was amplified compared to the original ion current as shown in Figure 22.

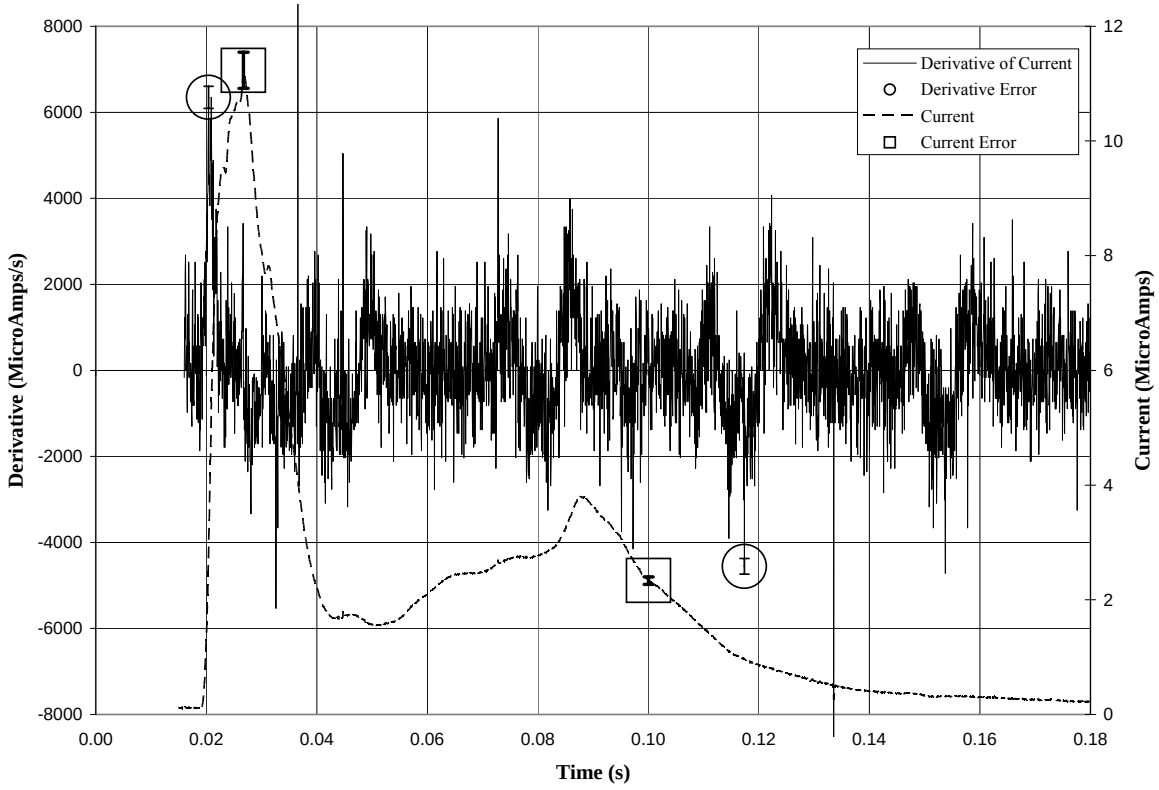

Figure 22. Current and derivative at baseline case

The resulting noisy derivative makes discerning useful information difficult at best. A limited time scale permits better resolution into the region of interest.

In order to extract information, a low-pass finite impulse response filter was applied using the remez function in MatLab. This filter was designed by using a

transition zone from 500 Hz to 1 kHz. In this manner unwanted noise above 1 kHz is eliminated but important characteristics of the signal remain as shown in Figure 23.

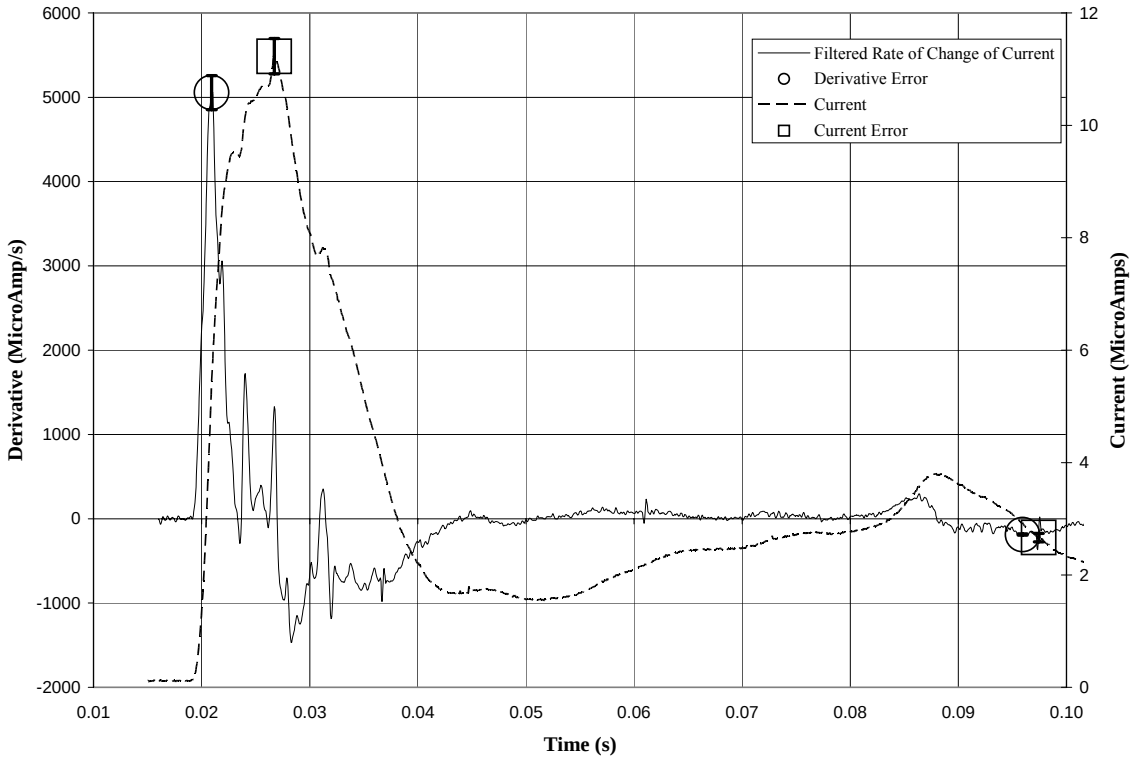

Figure 23. Filtered derivative and current at baseline case

Again the time scale is reduced to resolve the rate of change from the maximum current. By filtering the derivative, the noise is reduced but still shows some oscillatory behavior. The error bars show that although the error increases by taking the derivative, the error is still relatively small compared to the overall derivative level.

The repeatability of the filtered derivative is shown in Figure 24. Again some time variation occurs between each of the three runs. Peak levels also very between runs but similar behavior and patterns indict that signal is not random but contains useful reproducible information.

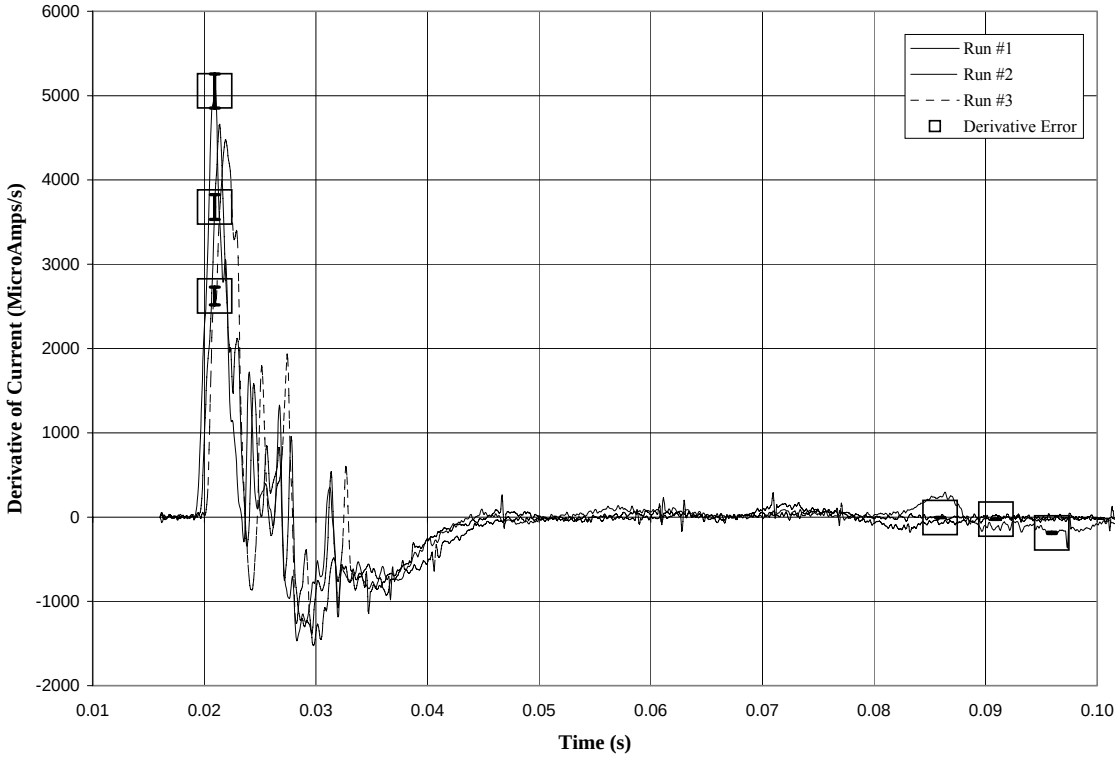

Figure 24. Repeatability of filtered derivative for 3 runs at baseline condition

How the derivative is affected by pressure is investigated in Figure 25. The area of interest in expanded in Figure 26.

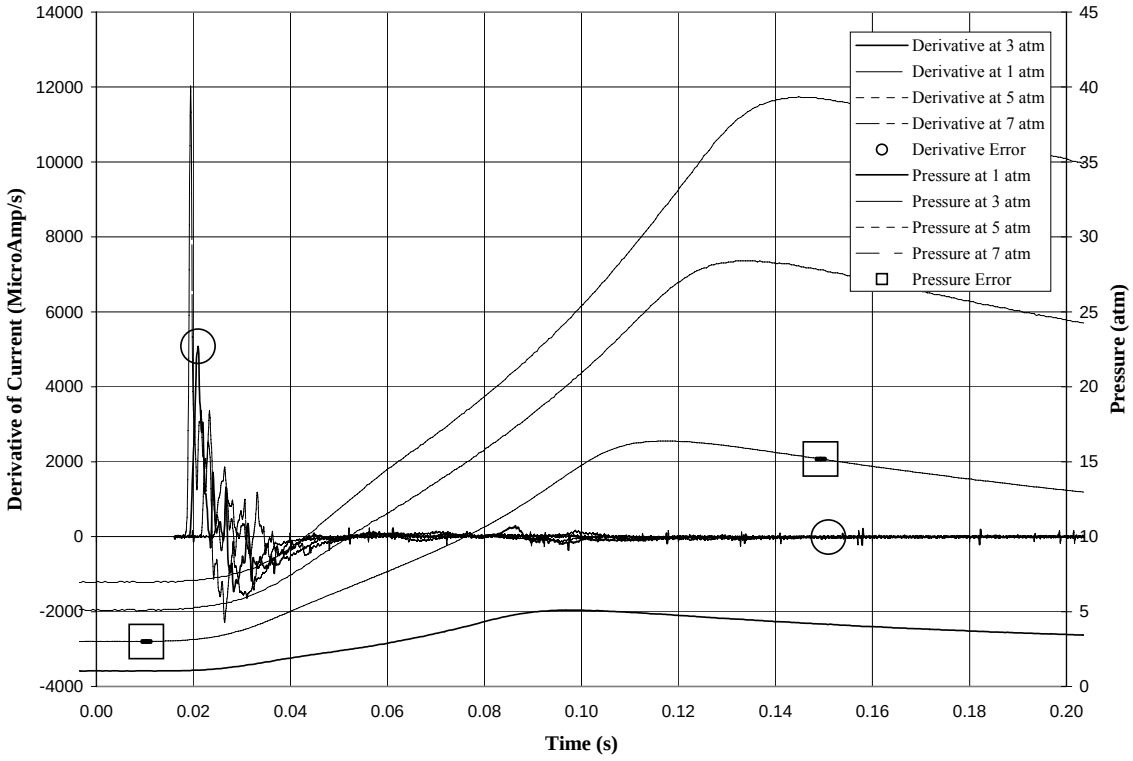

Figure 25. Filtered derivative compared for several initial pressures at φ = 1.0

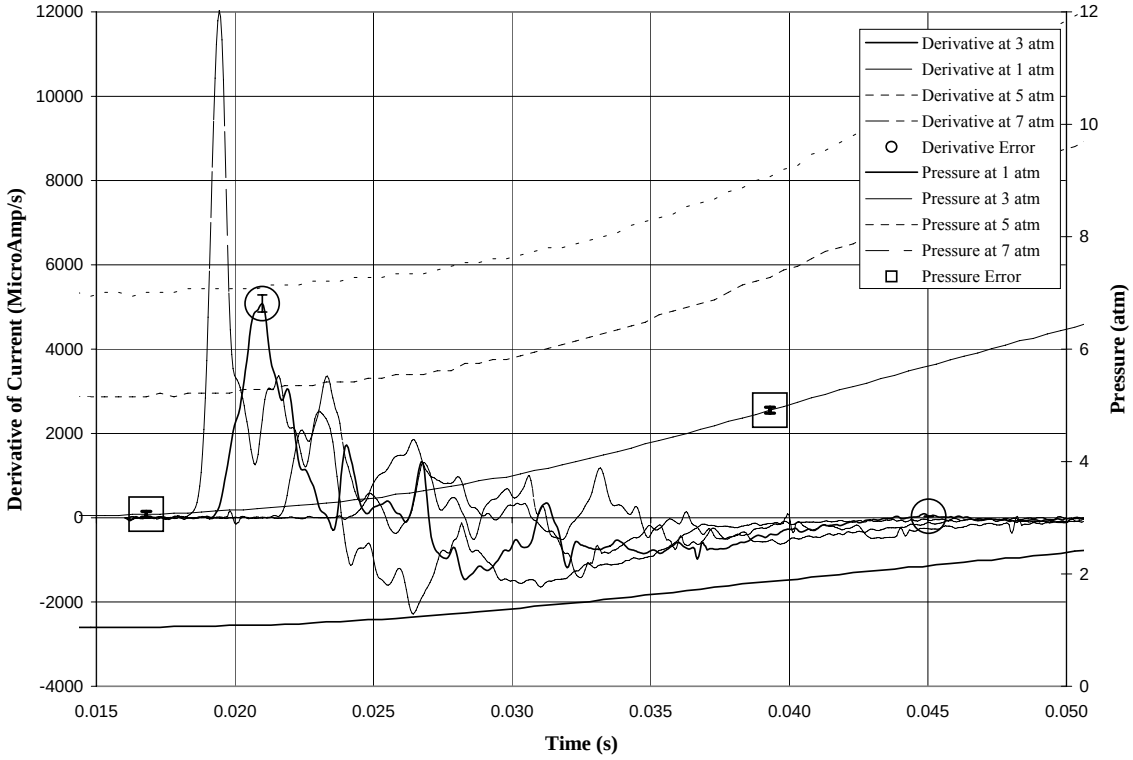

Figure 26. Expanded view of Figure 25 showing pressure affects on the derivative

The maximum positive level of the derivative clearly decreases at higher pressures. The minimum value of the derivative is not as clear but tends to increase with pressure. That is, the rate of ion current decay from the peak decreases with pressure.

V.5 Influence of Equivalence Ratio

Because the ion current depends upon the chemi-ionization process during combustion, the equivalence ratio is a critical factor for the ionization levels. As

previously discussed, the ion current was expected to decrease with lower equivalence ratios. The raw data presented in Chapter IV agreed with the trend to the extent that an ionization spike was nonexistent. By comparing the peak ion currents, this trend can be better understood as shown in Figure 27.

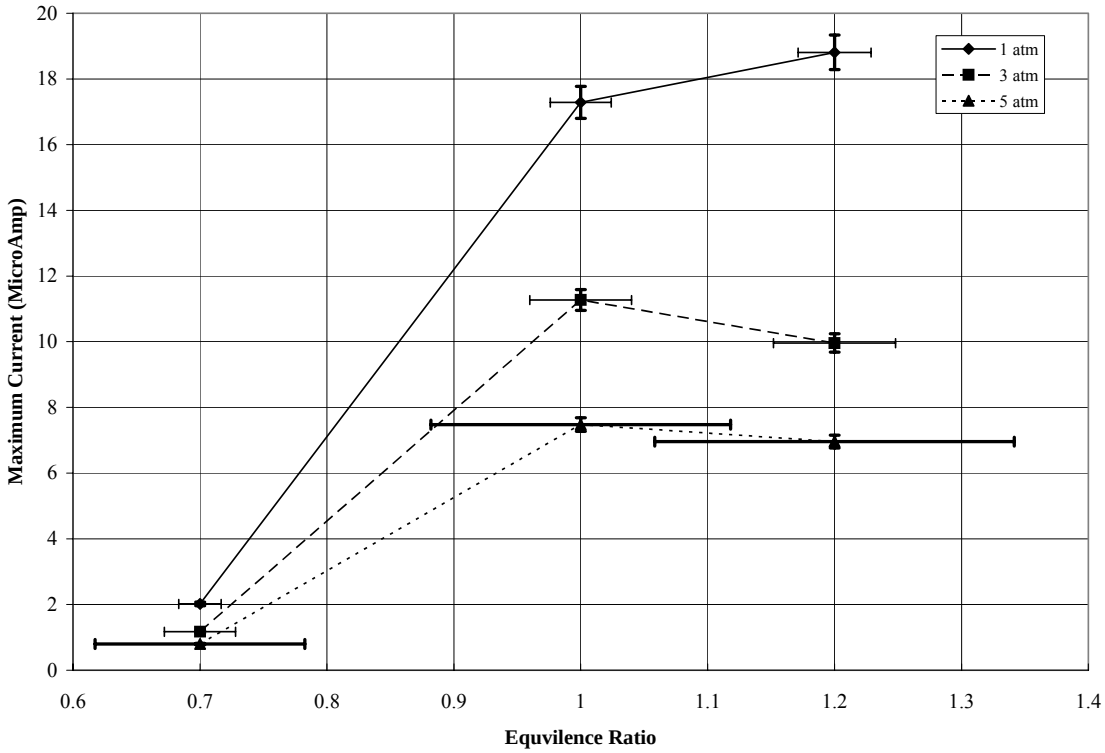

Figure 27. Effect of equivalence ratio on maximum ion current for initial pressures of 1, 3, & 5 atm

Because of the high relative error in the fuel partial pressure at 1 atm, the error in equivalence ratio is substantial. Despite this uncertainty, the ion current decreases sharply with lower equivalence ratios. At higher equivalence ratios, the ion current decreases

slightly for the 3 atm and 5 atm cases but increases for the 1 atm case. Since ion production requires both fuel and oxygen from equation 1, an ionization peak is expected near or above stoichiometric conditions. The limited number of tests run at various equivalence ratios provides little resolution into the exact location of this peak and how the location is affected by pressure.

The derivative of the current as a function of equivalence ratio can be examined in a similar fashion as shown in Figure 28.

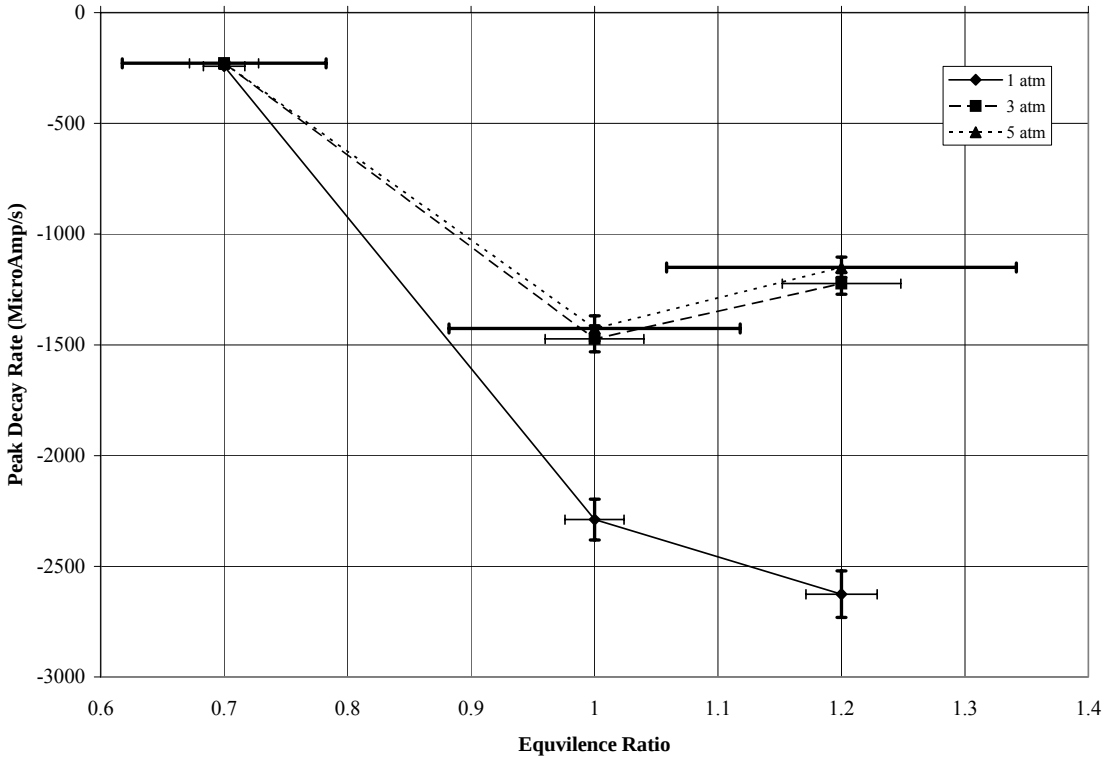

Figure 28. Peak decay rate of current as a function of equivalence ratio for initial pressures of 1, 3, & 5 atm

The peak decay rate or minimum negative derivative of the current occurs at stoichiometric conditions for the 3 atm and 5 atm cases but at an equivalence ratio of 1.2 for the 1 atm case. Compared to the maximum current, the peak decay rate shows the similar trends. That is, where the ion current was a maximum at stoichiometric conditions, the peak decay rate is also greatest at stoichiometric conditions.

The noise inherent in the derivative prevents useful examination of individual points. An average decay rate over a selected range also has limitations and is somewhat arbitrary. The peak ion current provides a clear starting point for the range, but a finding a suitable end point is challenging. Selecting the end point to be when the derivative equals zero creates easy calculations but the large time variance between test cases directly affects the result. End points based on other criteria are also highly variable because of both the noise and time variation in the signal. The parameter chosen to best quantify the derivative was the peak decay rate because of the relative consistency over several test runs.

V.6 Results as a Function of Pressure

Ultimately, the objective is to calculate the pressure by measuring the ion current. The theory of Chapter II states that the rate of change of the ion current, or decay rate, should be a function of pressure. The raw results of Chapter IV show that pressure has a strong influence on the peak ion current. The peak ion current averaged over three runs is compared to the pressure and shown in Figure 29.

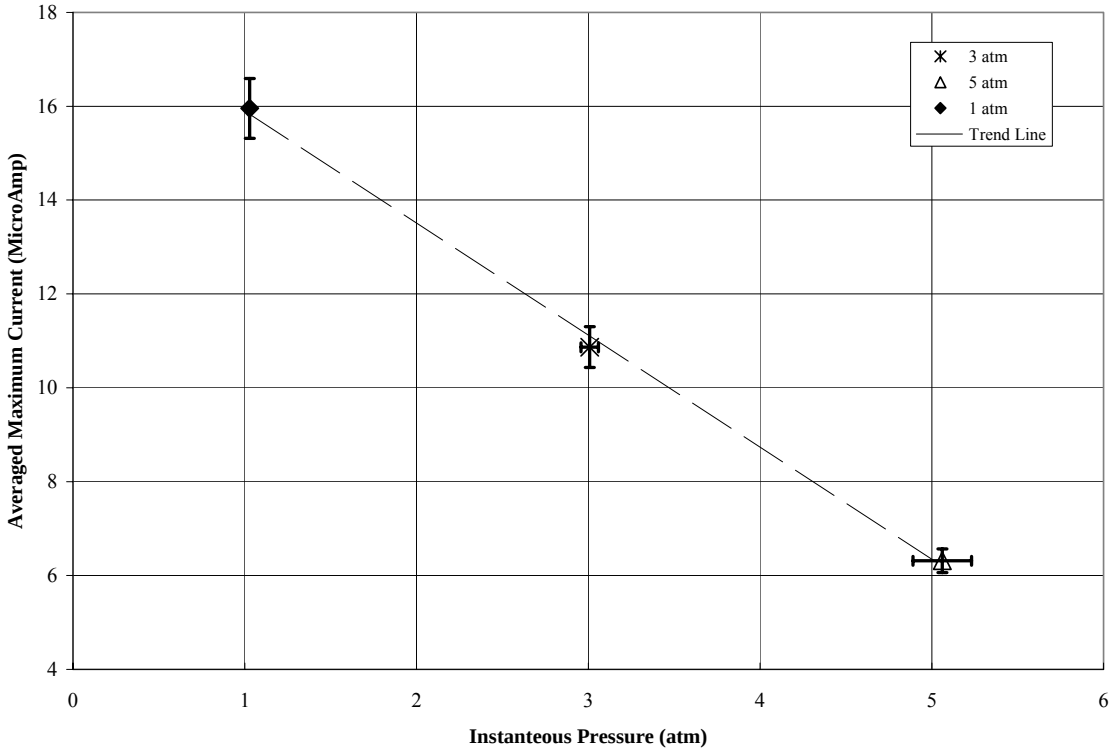

Figure 29. Maximum current averaged over three test runs plotted against the instantaneous pressure at $\varphi = 1.0$

The linear trend line in Figure 29, computed by the least squares method, shows a strong correlation with an R-squared value of 0.9982.

The computed linear trend is then compared to the individual cases as shown in Figure 30.

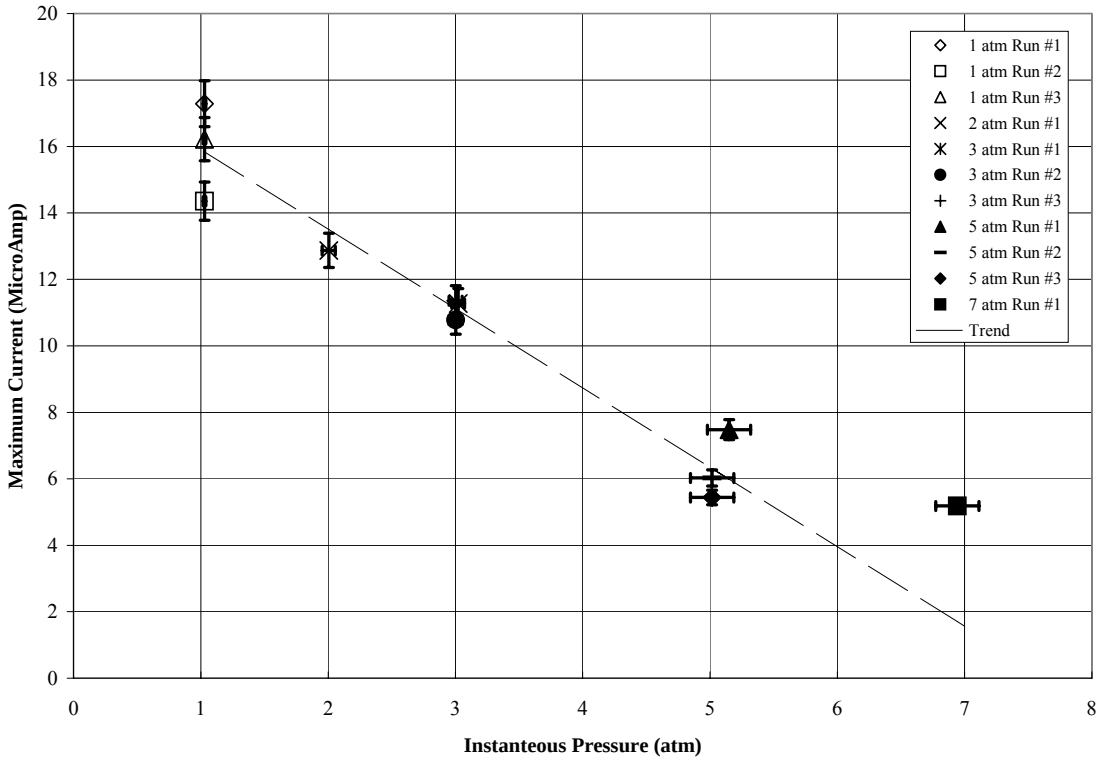

Figure 30. Maximum current for individual runs compared to pressure. The trend line shows the correlation computed from averaged cases

When compared against the individual test runs, the linear trend line is far less accurate.

The same approach is repeated for the derivative of the ion current. The peak decay rate averaged over three test runs is compared to the pressure as shown in Figure 31.

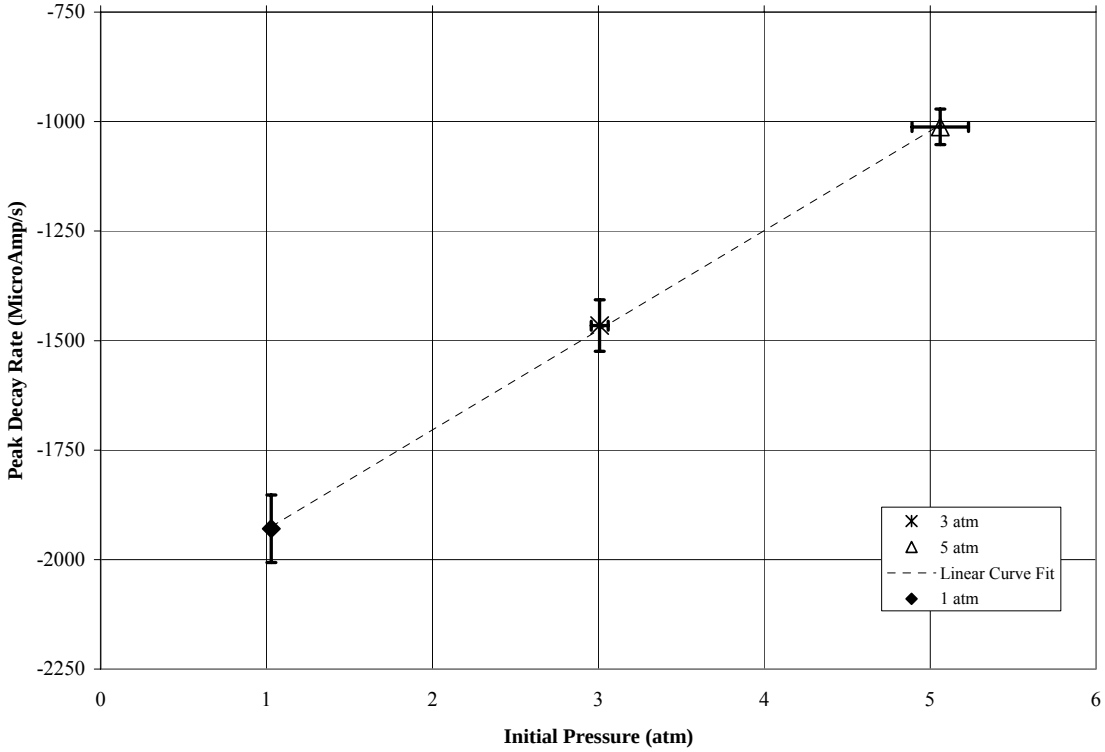

Figure 31. Peak decay rate averaged over three test runs and compared against instantaneous pressure for cases of φ = 1.0

Again, a linear trend line computed with the least squares method shows a good correlation between the pressure and the averaged peak decay rate with an R-squared value of 0.9997. Using this relationship to determine pressure, the resulting linear model is:

$$P = 0.0043964\frac{d(I_{mean})}{dt} + 9.491 \tag{22}$$

where $\left(\frac{dI}{dt}\right)_{mean}$ is the averaged peak decay rate in μA/s and P is the predicted pressure in atm. This linear model is only applicable to a pressure range from 1 atm to 5 atm at stoichiometric conditions. The usefulness of the model is also limited because the mean peak decay rate is required. This value is rarely available since actual conditions can vary for each measurement.

A more useful model can be devised by examining individual cases and not the mean peak decay rate. Again a linear correlation trend line is computed and the result, as shown in Figure 32, is similar to the previous correlation but the individual cases show greater variability.

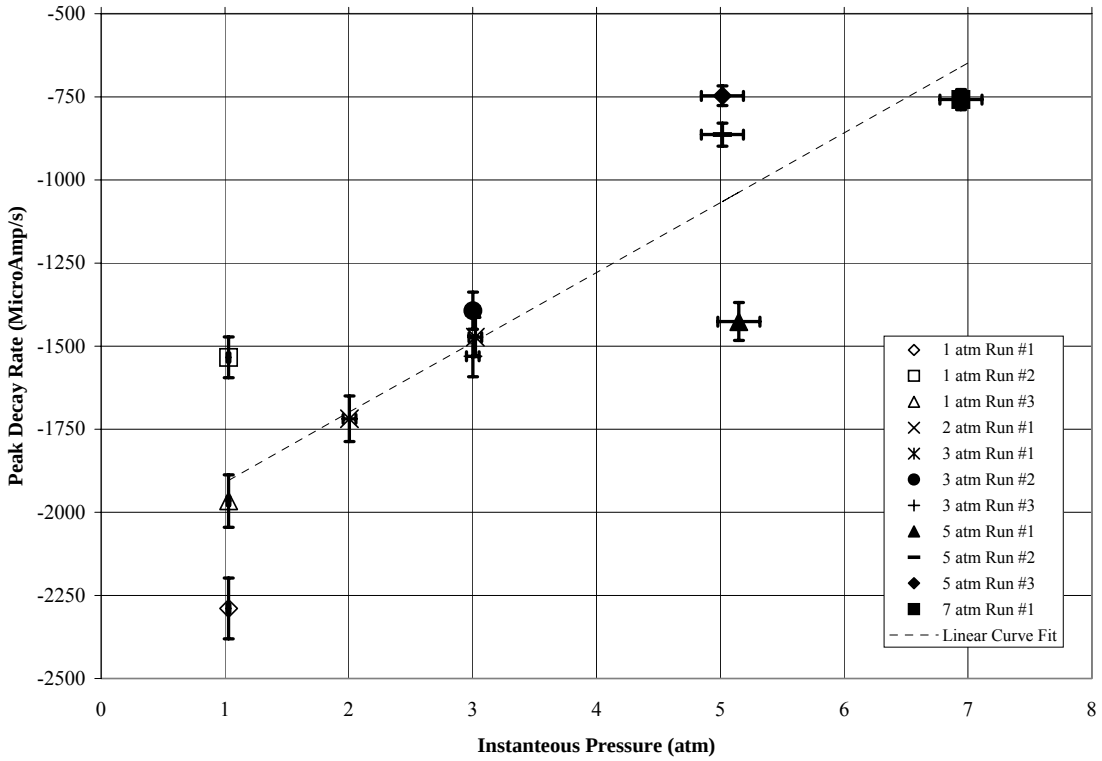

Figure 32. Peak decay rate for individual cases compared to the instantaneous pressure. A new correlation is computed.

The linear curve fit with an R-squared value of 0.7455 is not as accurate as the mean case. The variability of the peak decay rate with each test reduces the accuracy of the linear curve fit. A more useful linear model based on these individual cases is:

$$P = 0.0047515\frac{dI}{dt} + 10.084 \tag{23}$$

where $\frac{dI}{dt}$ is the peak decay rate in μA/s and P is the predicted pressure in atm. This linear model is only applicable to a pressure range from 1 atm to 7 atm at stoichiometric conditions.

The root mean square error (RMSE) is one useful metric to describe the error of the linear model. The definition of RMSE is:

$$RMSE = \sqrt{\frac{1}{n}\sum_{i=1}^{n}(x_i - a)^2} \tag{24}$$

where n is the number of samples, x_i is the value at sample i and a is the mean. Using the statistics software package JMP, the RMSE calculated for the linear model is 1.0635 atm. Although the accuracy of this linear model is less than desired, the model does show a strong, predictable relationship between the peak decay rate and pressure.

The linear model includes an intercept term that was not predicted by equations 19 & 20. Since the intercept term is on the same order as the slope term it can not be neglected. This term may be due to increasing ion recombination rates at higher pressures preventing the chemi-ionization from producing a super-equilibrium ion concentration. Near 10 atm, the ion recombination rate may match or exceed the ion production rate. This agrees with the expectation that the ion decay rate is a function of the square of pressure. This may limit the range of pressures that can be measured by this method. Nonetheless, this range is sufficient for capturing important pressures in the PDE.

V.7 Probe Resolution

The ion probe special resolution is on the same order of the diameter of the probe, approximately 0.3 cm. The time resolution of the probe can be approximated by:

$$t = \frac{v_{avg} m}{|q|E} \tag{25}$$

where t is the time, v_{avg} is the speed of sound (360 m/s), m is the mass of a molecule (4.84×10^{-26} kg for CHO^+), q is the elementary charge (1.60×10^{-19} C), and E is the applied electric field of 1.0 kV/m. The resulting response time is on the order of 100 nanoseconds or 10 MegaHertz (MHz).

The time and spatial resolution of the probe is adequate to observe the detonation wave structure and the following expansion zone in the PDE but not the von Neumann pressure spike.

VI. Conclusions

VI.1 Conclusions

The objective stated in Chapter I is to develop a new pressure sensor for the PDE based on work already accomplished in IC engines and the PDE itself. Chapter II predicts that the rate of change of the ion current decay rate should be a linear function of pressure. Inversely, pressure should be a linear function of the ion current decay rate. The results of Chapters IV and V show that both the ion current and the peak decay rate are a linear function of pressure. In other words, pressure is a linear function of the ion current and the peak decay rate. The theoretical prediction is generally correct in predicting a linear relationship despite variations in the ion current decay rate. The developed linear model in equation 23 provides an initial useful model for determining pressure although the accuracy needs to be improved. The intercept term in equation 23 may limit the useful range of this method.

The variations can be explained by several factors including local changes in equivalence ratio and non-uniform flame fronts. The derivation also did not account for additional forces and phenomena that can affect both the ion decay rate and the drift velocity. The instrumentation in the experimental setup, particularly the picoammeter, may not have been fast enough to correctly capture the transient events.

Interestingly, both the peak decay rate and the actual ion current showed a linear relationship with pressure. The IC engines only used the ion current to determine the pressure. As previously discussed, large variations in current can occur due to a number

of factors especially impurities. The derivative or peak decay rate method inherently increases the noise in the signal but offers a means of addressing problems with variations in the actual ion current. Although improved accuracy is required, this investigation conceptually shows the spark plug can provide an alternate method to measuring pressure in the PDE.

VI.2 Future Work

Future work will need a more detailed examination of the phenomena creating the relationship between pressure and the peak decay rate. Additional testing will be required to address other considerations such as different hydrocarbon fuels and impurities in the fuel. A larger set of test cases would help improve the usefulness of this method and accuracy of the model. Ultimately, the sensor will need to be compared to current pressure sensing methods within the PDE.

VI.3 Future Experimental Setup Recommendations

While the test setup was adequate for this initial investigation, subsequent work should improve this testing approach. Increasing the sample rate of the picoammeter would improve confidence that the transient events are correctly captured. This improvement will also be needed for the faster processing in the detonation cycle compared to the constant volume process investigated in this experiment. Also, to ease in data capture, a DAC capable of hardware triggering should replace the E-series card. This will release computer resources for better time resolution and improve time accuracy not only on that card but with the faster NI 6110 card as well. A faster computer is always desired but in this testing the limited 256 MB of memory was the biggest detriment.

The K-type thermocouple response time was too slow to provide much useful thermodynamic information other than initial temperature in the combustion bomb. A thermocouple with a smaller bead size would be much more useful.

The large errors in equivalence ratio at low pressure could easily be reduced by using additional pressure transducers to more accurately determine the partial and total pressures. A 5 psia transducer would be effective for measuring the vacuum and fuel partial pressures at low initial pressures. A 50 psia would be useful in reducing the error in the total pressure for the 2 atm and 3 atm test cases.

The variation in probe response with voltage was also not well understood. Saturation appeared to occur but the exact cause was not determined. Further investigation into the cause would also be useful in development of this method.

The poor wiring in the lab made creating a true ground impossible. Although efforts were taken to reduce noise as much as feasible, the experiment was still susceptible to noise from many sources.

Testing for a larger pressure range could also aid understanding and performance of the ion sensor. A larger number of cases at one condition would improve statistical confidence in the measurement.

Although some effort was made in selecting an appropriate filter for the ion current derivative, this method was not optimized nor was the effect of the filter fully taken into account during the data reduction.

The developed linear model works fairly well. A better statistical analysis with more data points could reveal a more accurate model as well as provided more insight into the dominant physical phenomena especially the intercept term.

Appendix A: LabView Program

LabView version 7.0 provided a quick and easy software package to collect the data. LabView has a large set of drivers to work with a variety of instruments and data acquisition cards. Initially, writing a LabView code was expected to be fairly straight forward because of all of its capabilities. Unfortunately, no pre-built Virtual Instruments (VI)s existed that performed all the required functions so a new VI had to be coded. The user friendly VIs built into LabView were too slow and limited to be useful for this experiment. A combination of higher level VIs was required to create the object oriented code. Newer drivers (LabView mx) were not yet written for the fast data acquisition card so the older traditional driver and VIs had to be used. The lack of hardware triggering in the E-series card required an elaborate VI intensive conditional triggering scheme as mentioned earlier. These complications turned the code into a substantial effort.

The coded program operated in two different modes. The first mode allowed for ensuring proper conditions before beginning the test. This mainly used continuous data acquisition VIs running at low data capture rates and displayed the results on the computer screen in real time as shown in Figure 33. To help determine sources of noise during the experimental setup, a FFT VI was used to show the current from the picoammeter in the frequency domain as shown in Figure 34. A simple digital band-gap filter VI was also tested but not used for data capture to reduce noise from the dominant 60 Hz sources. The detailed block diagram for the first mode is shown in Figure 35 and Figure 36.

The second program mode used a hardware trigger VI for the fast DAC and a conditional trigger VI for the E-series DAC. These VIs captured a set number of data

points before and after the trigger. After acquiring all the data, results were saved to a file and displayed on the screen as shown in Figure 37. Any errors the program encountered were also displayed. A time limit was also used for both these VIs to make sure the DACs did not go into a continuous loop looking for the trigger condition. The detailed block diagram for the second mode is shown in Figures 38 and Figure 39.

The program was switched from the first mode to the second mode by clicking on a Boolean button that moved the operation from one case structure to the other.

Figure 33. First program mode front panel

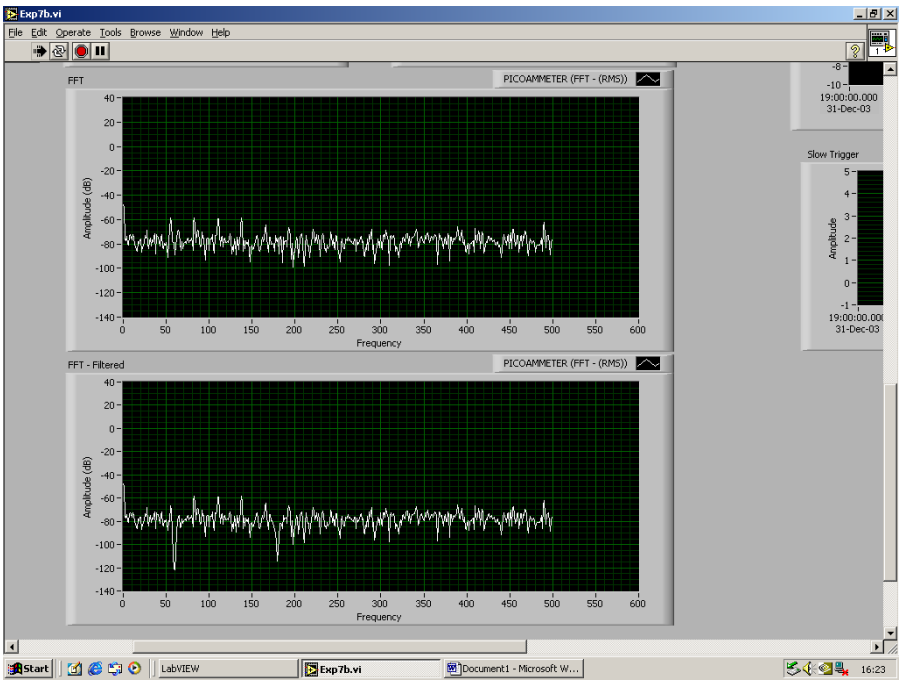

Figure 34. First mode front panel showing ion current in frequency domain

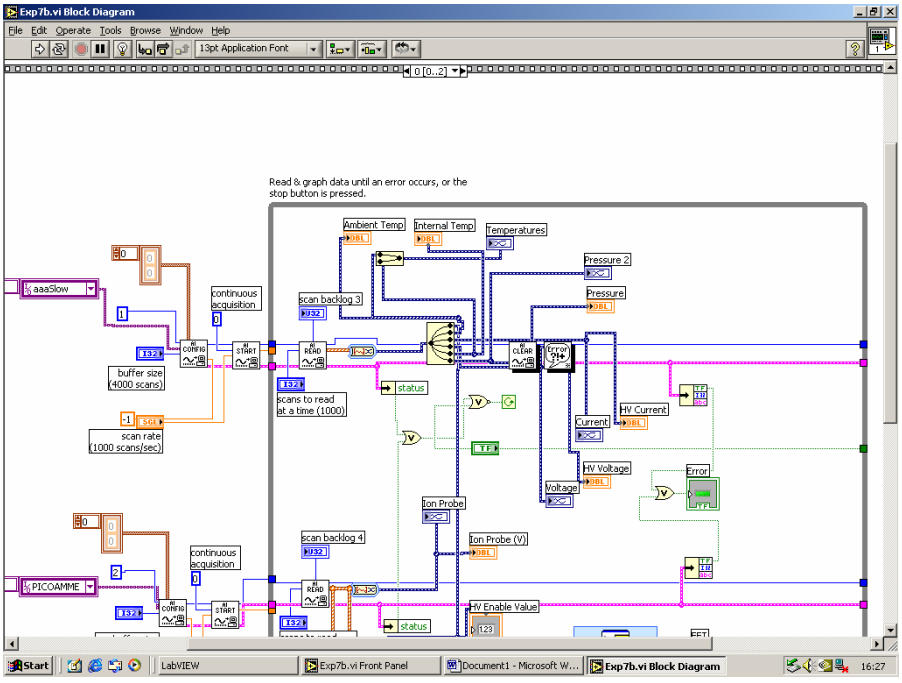

Figure 35. Top section of block diagram for first mode

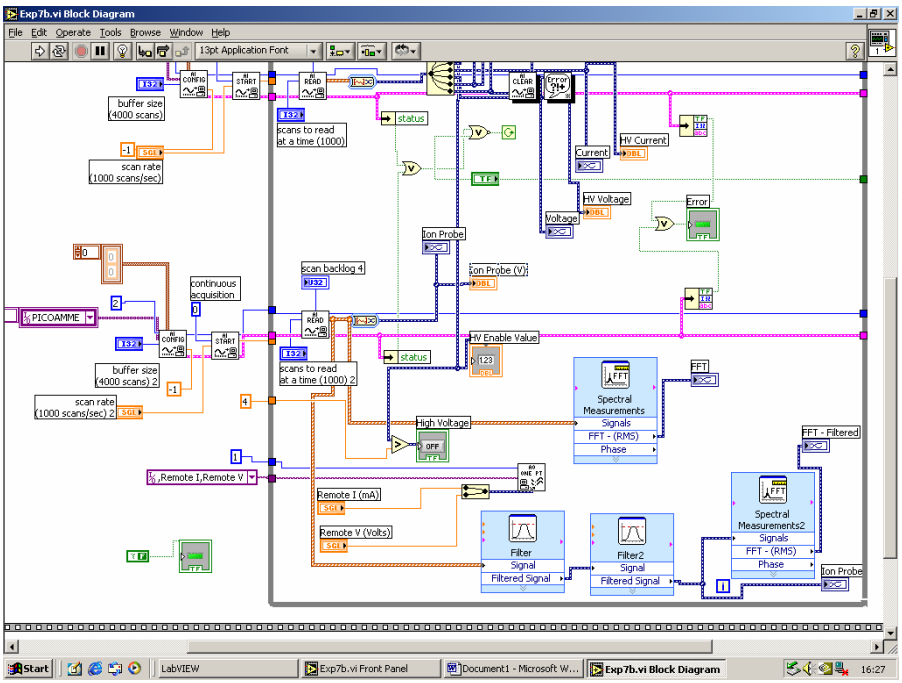

Figure 36. Bottom section of block diagram for first mode

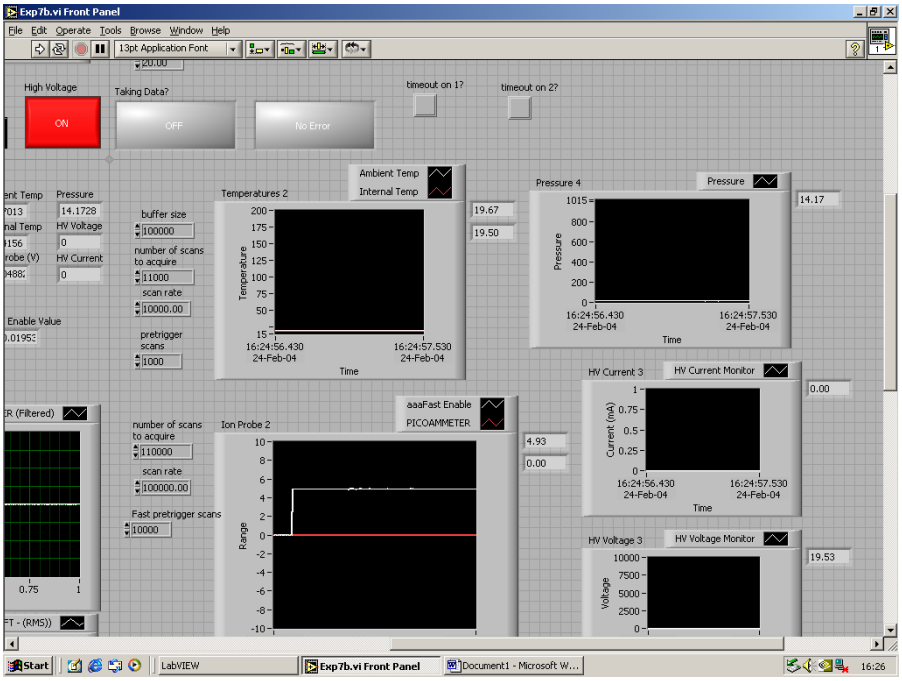

Figure 37. Front panel for second mode

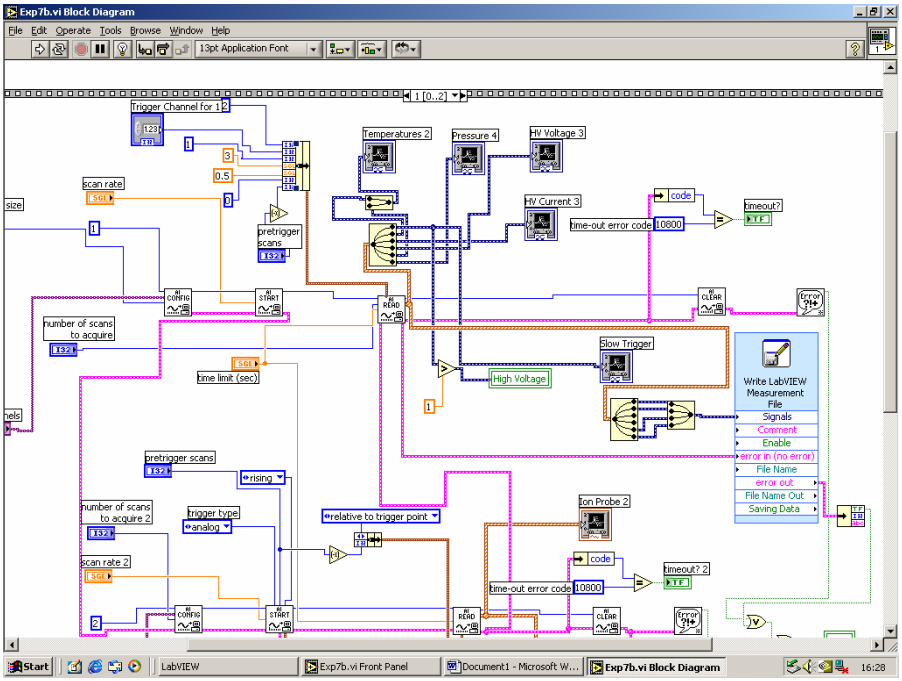

Figure 38. Top section of block diagram for second program mode

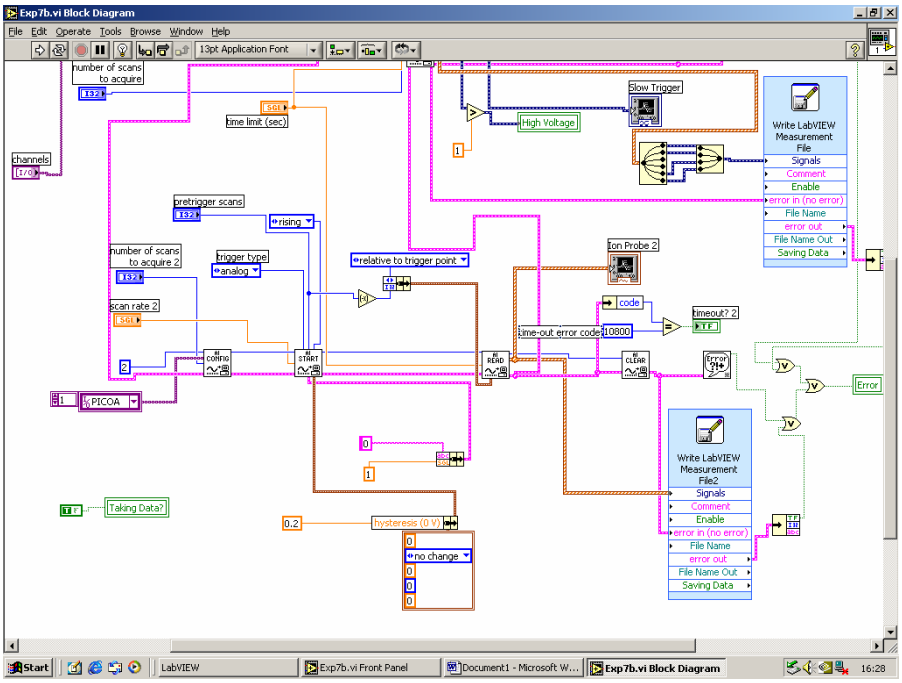

Figure 39. Bottom section of block diagram for second mode

Bibliography

1. Aithal, S.M., White, A.R., and Subramaniam, V.V., "Kinetic Modeling of an Ionization Sensor for Combustion Processes", 30th Plasmadynamics and Lasers Conference, Norfolk VA, 1999.

2. An, Fei, *Combustion Diagnostics in Methane-Fueled SI Engines Using the Spark Plug as an Ionization Probe*, MS Thesis, Ohio State University, 1996.

3. Auzins, J., Johansson, H. and Nytomt, J., "Ion-Gap Sense in Misfire Detection Knock and Engine Control", SAE-950004, 1995. (Reprinted from Electronic Engine Controls 1995 SP-1082).

4. Calcote, H.F., "Mechanisms for the Formation of Ions in Flames," *Combustion and Flame*, 1957, 1, 385-402

5. Calcote, H.F., "Ion Production and Recombination in Flames," *8th Int. Symposium on Combustion*, 1960, 184-199.

6. Coleman, M.L., *Overview of Pulse Detonation Propulsion Technology*, Chemical Propulsion Information Agency, CPTR 70, 2001.

7. Eriksson, L., and Nielsen, L., "Ionization Current Interpretation for Ignition Control in Internal Combustions Engines", *Control Eng. Practice*, 1997, Vol 5, No 8, 1107-1113.

8. Fialkov, A.B., "Investigation on Ions in Flames", *Prog. Energy Combust*. Sci.,1997, 23: 399-528.

9. Gord, J.R., and Fiechtner, G.J., "Emerging Combustion Diagnostics", 39th AIAA Aerospace Sciences Meeting & Exhibit, Reno, AIAA-2001-16608, 2001.

10. Hoke, J., Bradley, R., Schauer, F., "Heat Transfer and Thermal Management in a Pulsed Detonation Engine", 41th AIAA Aerospace Sciences Meeting & Exhibit, Reno NV, AIAA-2003-852, 2003.

11. Kailasanath, K., "Recent Developments in the Research on Pulsed Detonation Engines", 40th AIAA Aerospace Sciences Meeting & Exhibit, Reno NV, AIAA-2002-0470, 2002.

12. Kanury, A. M., *Introduction to Combustion Phenomena.* New York: Gorden and Breach Publishers, 1975.

13. Kentfield, J.A.C., "The Thermodynamics of Air-Breathing Pulse-Detonation Engines", 37th AIAA/ASME/SAE/ASEE Joint Propulsion Conference and Exhibit, Salt Lake City UT, AIAA-2001-3982, 2001.

14. Laderman, A.J., Hecht, G.J., Stern, R.A., and Oppenheim, A.K., "Flame Ionization During the Development of Detonation", *8th Int Symposium on Combustion*, 1960, 199-206.

15. Lee, A.T., Wilcutts, M., Tunestal, P., and Hedrick, J.K., "A Method of Lean Air-Fuel Ratio Control Using Combustion Pressure Measurement", *JSAE Review*, 2001, 22, 389-393.

16. Merer, R. M. and Wallace, J.S., "Spark Spectroscopy for Spark Ignition Engine Diagnostics," SAE-950164, 1995.

17. Miyata, S., Ito,Y., and Shimasaki, Y., "Flame Ion Density Measurement Using Spark Plug Voltage Analysis," SAE-930462, 1993.

18. Saitzkoff, A., Reinmann, R., Berglind, T., and Glavmo, M., "An Ionization Equilibrium Analysis of the Spark Plug as an Ionization Sensor," SAE-960337, 1996.

19. Saitzkoff, A., Reinmann, R., Mauss, F., and Glavmo, M., "In-Cylinder Pressure Measurements Using the Spark Plug as an Ionization Sensor," SAE-970857, 1997.

20. Schauer, F., Stutrud, J., Bradley, R., "Detonation Initiation Studies and Performance Results for Pulsed Detonation Engine Applications", 39th AIAA Aerospace Sciences Meeting & Exhibit, Reno NV, AIAA-2001-1129, 2001.

21. Shimasaki, Y., Kanehiro, M., Baba, S., Maruyama, S., Hisaki, T. and Miyata, S., "Spark Plug Voltage Analysis for Monitoring Combustion in an Internal Combustion Engine," SAE-930461, 1993.

22. Tucker, C., King, P., and Schauer, F. "Detonation Wave Speed Measurements with Ion Sensors", 28th Dayton-Cincinnati Aerospace Science Symposium, Dayton OH, March 2003.

23. Tucker, C., King, P., Schauer, F., and Hoke, J. "Branched Detonation in a Multi_Tube PDE ", 16th International Symposium on Air Breathing Engines, ISABE 2003-1218, Cleveland OH, September 2003.

24. Wheeler, A.J., Ganji, A.R. *Introduction to Engineering Experimentation.* New Jersey: Prentice Hall, 1995.

Vita

Capt Jeff Zdenek graduated from Riverside-Brookfield High School in Riverside, Illinois. He attended the University of Missouri - Rolla where he joined the Air Force ROTC program. In 1999 he graduated with a major in Aerospace Engineering and a minor in History.

Upon being commissioned as a 2nd Lt in the United States Air Force, Jeff was assigned to the DoD Space Test Program at Kirtland, AFB in Albuquerque, NM. He successfully led the Air Force portion of the joint NASA Kodiak Star mission to the first orbital launch from Kodiak, AK in September 2001. In the summer of 2002, he moved to Dayton, OH to attend the Air Force Institute of Technology to pursue a master's degree in aeronautical engineering. Upon graduation, he will be assigned to the Air Force Research Lab, Air Vehicles Directorate.

REPORT DOCUMENTATION PAGE

Form Approved
OMB No. 074-0188

1. REPORT DATE *(DD-MM-YYYY)*	2. REPORT TYPE	3. DATES COVERED *(From – To)*
12-03-2004	Master's Thesis	March 2003 – March 2004

4. TITLE AND SUBTITLE

ION BASED PRESSURE SENSOR FOR PULSE DETONATION ENGINES

5a. CONTRACT NUMBER

5b. GRANT NUMBER

5c. PROGRAM ELEMENT NUMBER

6. AUTHOR(S)

Zdenek, Jeffrey S., Captain, USAF

5d. PROJECT NUMBER

5e. TASK NUMBER

5f. WORK UNIT NUMBER

7. PERFORMING ORGANIZATION NAMES(S) AND ADDRESS(S)

Air Force Institute of Technology
Graduate School of Engineering and Management (AFIT/ENY)
2950 Hobson Way, Building 641
WPAFB OH 45433-7765

8. PERFORMING ORGANIZATION REPORT NUMBER

AFIT/GAE/ENY/04-M17

9. SPONSORING/MONITORING AGENCY NAME(S) AND ADDRESS(ES)

Dr. Robert Hancock, AFRL/PRTS
1950 5th St
WPAFB, OH 45433-7251

10. SPONSOR/MONITOR'S ACRONYM(S) AFRL/PRTS

11. SPONSOR/MONITOR'S REPORT NUMBER(S)

12. DISTRIBUTION/AVAILABILITY STATEMENT

APPROVED FOR PUBLIC RELEASE; DISTRIBUTION UNLIMITED.

13. SUPPLEMENTARY NOTES

14. ABSTRACT

A high speed, durable, ion probe based pressure sensor is being investigated for use in pulse detonation engines. Traditional pressure sensors are ill suited for the high temperature and vibratory environment encountered in such engines. An alternative transient pressure sensing method is investigated for pressures behind a hydrocarbon flame. These flames generate ions that are quenched by collisions as a function of pressure. An experiment was devised to correlate the ion decay rate with the pressure using an ion probe well suited for the flow. A correlation has been established showing the ion decay rate is a function of pressure. Additional investigation is required even though the ion probe remains a viable alternative method for measuring pressure.

15. SUBJECT TERMS

Pressure, Sensor, Pulse Detonation Engine, Ion

16. SECURITY CLASSIFICATION OF:			17. LIMITATION OF ABSTRACT	18. NUMBER OF PAGES	19a. NAME OF RESPONSIBLE PERSON
a. REPORT	b. ABSTRACT	c. THIS PAGE			Ralph A. Anthenien
U	U	U	UU	113	19b. TELEPHONE NUMBER *(Include area code)* (937) 255-6565, ext 4643 (Ralph.Anthenien@afit.edu)